Ore Geology Reviews 73 (2016) 148–174

Contents lists available at ScienceDirect

Ore Geology Reviews

journal homepage: www.elsevier.com/locate/oregeorev

The application of S isotopes and S/Se ratios in determining ore-forming processes of magmatic Ni–Cu–PGE sulfide deposits: A cautionary case study from the northern Bushveld Complex

Jennifer W. Smith [a,b], David A. Holwell [a,*], Iain McDonald [c], Adrian J. Boyce [d]

[a] Department of Geology, University of Leicester, University Road, Leicester, LE1 7RH, UK
[b] AMTEL, 100 Collip Circle, Suite 205, University of Western Ontario Research Park, London, Ontario N6G 4X8, Canada
[c] School of Earth and Ocean Sciences, Cardiff, University, Park Place, Cardiff CF10 3YE, UK
[d] Scottish Universities Environmental Research Centre, Rankine Avenue, Scottish Enterprise Technology Park, East Kilbride, G75 0QF, UK

ARTICLE INFO

Article history:
Received 17 March 2015
Received in revised form 16 October 2015
Accepted 20 October 2015
Available online 22 October 2015

Keywords:
Magmatic sulfides
S/Se ratios
S isotopes
Bushveld Complex
GNPA member
Platreef

ABSTRACT

The application of S/Se ratios and S isotopes in the study of magmatic Ni–Cu–PGE sulfide deposits has long been used to trace the source of S and to constrain the role of crustal contamination in triggering sulfide saturation. However, both S/Se ratios and S isotopes are subject to syn- and post-magmatic processes that may alter their initial signatures. We present in situ mineral $\delta^{34}S$ signatures and S/Se ratios combined with bulk S/Se ratios to investigate and assess their utility in constraining ore-forming processes and the source of S within magmatic sulfide deposits.

Magmatic Ni–Cu–PGE sulfide mineralization in the Grasvally Norite–Pyroxenite–Anorthosite (GNPA) member, northern Bushveld Complex was used as a case study based on well-defined constraints of sulfide paragenesis and local S isotope signatures. A crustal $\delta^{34}S$ component is evident in the most primary sulfide assemblage regardless of footwall lithology, and is inferred that the parental magma(s) of the GNPA member was crustally contaminated and sulfide saturated at the time of emplacement. However, S/Se ratios of both the primary and in particular secondary sulfide assemblages record values within or below the mantle range, rather than high crustal S/Se ratios. In addition, there is a wide range of S/Se ratio for each sulfide mineral within individual assemblages that is not necessarily consistent with the bulk ratio. The initial crustal S/Se ratio is interpreted to have been significantly modified by syn-magmatic lowering of S/Se ratio by sulfide dissolution, and post-magmatic lowering of the S/Se ratio from hydrothermal S-loss, which also increases the PGE tenor of the sulfides. Trace element signatures and variations in Th/Yb and Nb/Th ratios support both an early pre-emplacement contamination event as seen by the S isotopes and S/Se ratios, but also a second contamination event resulting from the interaction of the GNPA magma with the local footwall country rocks at the time of emplacement; though this did not add any additional S. We are able to present an integrated emplacement and contamination model for the northern limb of the Bushveld Complex.

Although the multitude of processes that affect variations in the $\delta^{34}S$ signature and in particular S/Se ratio may be problematic in interpreting ore genesis, they can reveal a wealth of additional detail on a number of processes involved in the genetic history of a Ni–Cu–PGE deposit in addition to crustal contamination. However, a prerequisite for being able to do this is to utilize other independent petrological and mineralogical techniques that provide constraints on both the timing and effect of various ore-forming and modifying processes. Utilizing both bulk and in situ methods in concert to determine the S/Se ratio allows for the assessment of multiple sulfide populations, the partitioning behaviour of Se during sulfide liquid fractionation and also the effects of low temperature fluid alteration. In comparison, S isotopes are relatively more robust and represent a more reliable indicator of the role of crustal S contamination. The addition of trace element data to the above makes for an incredibly powerful approach in assessing the role of crustal contamination in magmatic sulfide systems.

1. Introduction

Magmatic sulfide deposits of Ni, Cu and platinum-group elements (PGE) form when mafic/ultramafic magmas become saturated in sulfide, and an immiscible sulfide liquid scavenges chalcophile metals

* Corresponding author.
E-mail address: dah29@le.ac.uk (D.A. Holwell).

http://dx.doi.org/10.1016/j.oregeorev.2015.10.022

from the silicate magma (e.g. Naldrett, 2011). While some S is present within such magmas from melting of their mantle sources, many consider the addition of S via assimilation of S-bearing country rocks critical in triggering the generation of large magmatic ore deposits such as Noril'sk and Voisey's Bay (e.g. Grinenko, 1985; Lesher, 1986; Lesher and Burnham, 2001; Lesher and Keays, 2002; Li et al., 2002; Lightfoot and Keays, 2005). Sulfur/selenium ratios and S isotopes have long been used to investigate the source of S in magmatic sulfide deposits to constrain the role of crustal contamination in ore genesis (e.g. Eckstrand and Cogolu, 1986; Eckstrand et al., 1989; Peck and Keays, 1990; Ripley, 1990; Thériault and Barnes, 1998; Holwell et al., 2007; Ihlenfeld and Keays, 2011; Sharman et al., 2013). In addition, a number of trace element ratios and patterns can be used to determine crustal contamination in more broad terms, not specific to addition of S (e.g. Lightfoot and Hawkesworth, 1988; Lightfoot et al., 1990).

The S/Se ratio of the mantle is well-constrained at 2850–4350 (Eckstrand and Hulbert, 1987), with average values indicated by McDonough and Sun (1995); Hattori et al. (2002) and Lorand et al. (2003) of 3333, 3300 and 3150, respectively. The mantle values are slightly elevated from chondritic values, reported by Dreibus et al. (1995) to be 2500 ± 270 in meteorites. The mantle also exhibits a constrained $\delta^{34}S$ signature of 0 ± 2‰ (Ohmoto and Rye, 1979). In comparison, crustal rocks may exhibit $\delta^{34}S$ values in the range of <−40‰ to >+30‰ and mostly have S/Se ratios of 3500 to 100,000 (Yamamoto, 1976). Therefore, magmatic Ni–Cu–PGE deposits characterized by S/Se ratios and $\delta^{34}S$ values within or close to the mantle range can be interpreted to have S of mantle origin (e.g. Buchanan et al., 1981; Barnes et al., 2009). In contrast, S/Se ratios exceeding the mantle range or $\delta^{34}S$ signatures distinct from that of mantle S can be used to signify a substantial contribution of externally derived S (e.g. Thériault and Barnes, 1998; Lesher and Burnham, 2001; Ihlenfeld and Keays, 2011).

In recent years, however, it has become apparent that the interpretation of S/Se ratios, and to a lesser extent S isotope signatures, in terms of the input of crustal S, is subject to a number of uncertainties, implemented primarily by the ability of syn- and post-magmatic processes to modify the initial values of both indicators. For S/Se ratios these modifying processes include: variations in the sulfide to silicate ratio (R-factor; Queffurus and Barnes, 2015); preferential retention of Se in the mantle during partial melting (Hattori et al., 2002); 'multistage-dissolution upgrading' which involves partially dissolving sulfide at depth (e.g. Kerr and Leitch, 2005; Holwell et al., 2011; McDonald et al., 2012; Holwell et al., 2014); apparent fractionation of Se between monosulfide solid solution and intermediate solid solution (Helmy et al., 2010); metamorphism (Queffurus and Barnes, 2015) and post-magmatic S-loss (Yamamoto, 1976; Howard, 1977). In addition, a number of processes are known to affect S isotope compositions, including magma degassing, changes in magma redox state, fractionation by crystallization of sulfide at different temperatures (Ohmoto and Rye, 1979) and S isotope exchange between the crustally contaminated sulfide liquid and mantle S (Ripley and Li, 2003); though these are thought to have a much more restricted modifying effect than those affecting S/Se ratios.

Until recently (e.g. Prichard et al., 2013; Dare et al., 2014; Holwell et al., in press), the Se concentration of sulfides could not be determined accurately using in situ techniques, and so previous studies utilized S/Se ratios that were representative of bulk rock values (e.g. Ripley, 1990; Thériault and Barnes, 1998; Ripley et al., 2002; Hinchey and Hattori, 2005; Ihlenfeld and Keays, 2011; Holwell et al., 2014). In this paper we determine Se contents of sulfides by laser ablation-inductively coupled plasma-mass spectrometry (LA-ICP-MS) in addition to bulk rock concentrations and, for the first time, combine these with a detailed $\delta^{34}S$ study to establish whether the effects of a variety of processes modify these indicators independently. We also utilize trace element geochemistry as a separate, independent indicator of crustal contamination. Together, these integrated techniques make a powerful approach to the assessment of contamination in the development of magmatic sulfide deposits.

We use a magmatic sulfide deposit from the northern limb of the Bushveld Complex; the Grasvally Norite-Pyroxenite-Anorthosite (GNPA) member, where a number of magmatic and hydrothermal processes are well constrained (Smith et al., 2011, 2014; Maier et al., 2008) as a case study. In doing so, we are able to assess the utility of S/Se ratios and S isotopes on a mineralogical versus bulk rock scale in constraining ore-forming processes. In particular, we show that they can be used to elucidate a number of syn-and post magmatic processes in addition to providing evidence for the source of S. Furthermore, we highlight why an appreciation of these other processes is required to be able to fully apply S/Se ratios and S isotopes to the interpretation of crustal contamination.

2. The S/Se ratios of magmatic sulfides

A number of studies have all constrained the mantle range of S/Se ratios to be close to that defined by Eckstrand and Hulbert (1987) as 2850–4350, with McDonough and Sun (1995); Hattori et al. (2002) and Lorand et al. (2003) all calculating averages around 3250. Thus, magmatic sulfides with S/Se ratios within this range can generally be interpreted to have S mostly of mantle origin. Crustal rocks have S/Se ratios higher than the mantle range, <100,000 (Yamamoto, 1976), and so contaminated magmatic sulfides will generally show S/Se ratios higher than those of the mantle. Critically, however, initial magmatic S/Se ratios can be modified by a number of processes (Queffurus and Barnes, 2015), thus masking or eradicating the evidence traditionally used for interpreting contamination effects. While this makes contamination studies more complex, it illustrates that S/Se ratios can actually be used much wider in the identification of a number of syn- and post-magmatic processes.

Due to the chalcophile nature of elements such as Se and PGE, their concentration in sulfide is primarily dependent on the ability of the sulfide liquid to effectively interact with a large volume of silicate magma (i.e. the R-factor). The sulfide/silicate melt partition coefficient ($D_{sul/sil}$) of the PGE ranges from 17,000 to 92,000 (Naldrett, 2011 and references therein) and possibly up to 500,000 for Pd (Mungall and Brenan, 2014). Although Patten et al. (2013) report a $D_{sul/sil}$ value of 323 for Se, it is more generally accepted that the $D_{sul/sil}$ value applicable to most magmatic sulfide systems is closer to those calculated by Peach et al. (1990) and Brenan (2015) of 1700 and 1388, respectively. Variations in R-factor will also have an effect on the Se concentration of a sulfide and thus also its S/Se ratio (e.g. Thériault and Barnes, 1998; Ihlenfeld and Keays, 2011). To illustrate, an increase in R-factor will further enrich the sulfide liquid in PGE and Se, thus producing sulfides characterized by very high PGE and relatively high Se tenors and low S/Se ratios (i.e. potentially lower than the mantle range; Queffurus and Barnes, 2015).

Low S/Se ratios combined with high PGE tenors can also potentially be generated through a process termed 'multistage-dissolution upgrading' (Kerr and Leitch, 2005) where sulfides may be partially dissolved as multiple batches of S-undersaturated magma interact with sulfide liquid. This process is analogous to an increase in R-factor, upgrading metal tenors of elements with high ($D_{sul/sil}$), including the PGE and Se. Conversely, elements with low partition coefficients such as Fe and S will be preferentially resorbed by the magma thus the highest PGE tenor sulfides will exhibit the lowest S/Se ratios. Consequently, variations in R-factor and sulfide dissolution may mask or reduce an initial crustal or even mantle signature (e.g. Merensky Reef, Naldrett et al., 2009; Platreef, McDonald et al., 2012; River Valley Intrusion, Ontario, Holwell et al., 2014).

In addition, the Se contents of the initial silicate magma may also be modified during crystallization through early extraction of a sulfide liquid from the silicate magma. Due to the relatively high $D_{sul/sil}$ of Se, this effectively depletes the remaining silicate magma in Se, increasing the S/Se ratio to crustal-like values in the overlying cumulates (Barnes et al., 2009); analogous to Cu/Pd ratio increases (Maier et al., 1996).

Furthermore, due to the apparent preferential retention of Se over S in the mantle the initial Se concentration and thus S/Se values of mantle derived magmas may also vary depending on the degree of partial melting and previous melting history of the mantle source (Hattori et al., 2002; Lorand et al., 2013). Thus magmas derived through re-melting of the mantle are considered capable of producing very low S/Se ratios (<1000) as the magma is depleted in S and enriched in Se (Hattori et al., 2002).

Sulfur/selenium ratios can also be modified further by late stage- to post-magmatic processes including: low temperature hydrothermal alteration; supergene weathering; serpentinization and metamorphism (Queffurus and Barnes, 2015). As S is relatively more mobile than Se in hydrothermal fluids below temperatures of around 500 °C (Ewers, 1977) and is thus preferentially incorporated into aqueous fluids (Yamamoto, 1976; Howard, 1977), all of these fluid processes can result in preferential S-loss leading to a lowering of S/Se ratios (e.g. Peck and Keays, 1990; Cawthorn and Meyer, 1993; Maier and Barnes, 1996; Ripley et al., 2002; Hinchey and Hattori, 2005).

3. The S isotope composition of magmatic sulfides

The $\delta^{34}S$ signatures of sulfides in a magmatic sulfide deposit should reflect a magmatic, or mantle, signature of $0 \pm 2‰$ if the S in the sulfide is primarily sourced from the magma from which it separated. However, sulfides with $\delta^{34}S$ compositions that deviate from that of mantle S are often attributed to have incorporated S from a crustal source, with black shales and evaporites among the most common contributors of crustal S (e.g. Ripley and Li, 2003; Penniston-Dorland et al., 2012). The role of crustal contamination can, however, only be assessed if the isotopic composition of the country rock S is distinct from that of the local mantle. Since the bacterial processes (biologically mediated reduction of sulfate, e.g. Chambers and Trudinger, 1979; Habicht and Canfield, 1997) responsible for much of the S isotope fractionation found in sedimentary rocks were not established until around 2.7 Ga, all Archaean rocks older than this contain $\delta^{34}S$ similar to the mantle range (Grassineau et al., 2005).

In addition to the assimilation of S-bearing country rocks, S isotope variations in mafic magmas may also be caused by magma degassing associated with low pressure emplacement, changes in the redox state of the magma, fractionation by crystallization of sulfide at different temperatures (Ohmoto and Rye, 1979) and S isotope exchange between the crustally contaminated sulfide liquid and mantle S (Ripley and Li, 2003). While the effects of the former three processes on $\delta^{34}S$ values are considered negligible (up to 1‰ fractionation; Ohmoto and Rye, 1979; Miyoshi et al., 1984; Ripley and Li, 2003, and references therein), S isotope exchange may be capable of masking or eliminating an initial crustal $\delta^{34}S$ signature and thus evidence of the earliest stage of ore genesis (e.g. Platreef; Ihlenfeld and Keays, 2011). In deposits which have experienced multiple contamination events (pre-, syn- and post- emplacement), the initial isotope composition of the sulfide liquid may also be erased or overprinted by later, localised contamination through the addition of crustal S that is distinct in its isotopic composition (e.g. Platreef; Holwell et al., 2007; Ihlenfeld and Keays, 2011; Sharman et al., 2013).

4. The grasvally norite–pyroxenite–anorthosite member

The 400–800 m thick GNPA member is located in the northern limb of the Bushveld Complex, south of the Ysterberg–Planknek Fault and lies at the equivalent stratigraphic position to the Platreef, being overlain by Main Zone cumulates of the Rustenburg Layered Suite (Fig. 1). It is underlain by Lower Zone cumulates west of the Grasvally Fault and Paleoproterozoic Transvaal Supergroup sediments comprised of the Magaliesberg Quartzite Formation to the east (Fig. 1). The GNPA member comprises vari-textured gabbronorites, norites, anorthosites, pyroxenites and at least one PGE-bearing chromitite (Hulbert, 1983; Smith et al., 2011) and is typically sub-divided into three distinct stratigraphic units (de Klerk, 2005): the Lower Mafic Unit (LMF); the Lower Gabbronorite Unit (LGN); and the Mottled Anorthosite Unit (MANO). The LMF is distinguished from the homogeneous gabbronorites of the LGN by elevated bulk Cr values. The MANO is recognised by a substantial increase in plagioclase cumulates and the development of lithologies such as mottled and spotted anorthosites (Hulbert, 1983; Smith et al., 2011). The LGN, which is completely barren of PGE-bearing sulfides, is thought to represent a sill of Main Zone rocks (de Klerk, 2005). Detailed descriptions on the geology of the succession and associated PGE and BMS mineralization are provided in Hulbert (1983); McDonald et al. (2005); Maier et al. (2008) and Smith et al. (2011, 2014).

4.1. Sulfide mineralogy

The observed distribution and mineralogy of sulfides and PGE results from processes of both magmatic sulfide fractionation and low temperature (<230 °C) fluid alteration (Fig. 2; Smith et al., 2011, 2014). In places, a primary pyrrhotite–pentlandite–chalcopyrite sulfide assemblage (Fig. 2A) has been replaced to varying extents by a low temperature assemblage of pyrite, millerite and chalcopyrite (Fig. 2B and C). The degree of replacement varies significantly throughout the succession and can be viewed as a continuum from a purely magmatic sulfide assemblage to almost completely replaced sulfides (Fig. 2; Smith et al., 2011). Remobilization and redistribution of PGE is limited, with some platinum-group minerals (PGM) recrystallization in situ and pyrite and millerite inheriting PGE contents of the phases replaced (Fig. 2; Smith et al., 2014). The underlying Magaliesberg Quartzites contain some sedimentary pyrite, which is texturally distinct from the sulfide of magmatic assemblage that has infiltrated the floor rocks (Smith et al., 2011).

4.2. Justification as a case study

The GNPA member represents a favourable case study for several reasons. Firstly, the sulfide mineralization has been studied in detail, in terms of mineralogy, distribution and hydrothermal interaction (Smith et al., 2011, 2014), enabling the effects of secondary alteration to be easily identified and thus considered in any interpretation. The well-defined primary sulfide assemblage and low temperature hydrothermal overprint provide the opportunity to assess in detail the partitioning behaviour of Se during sulfide fractionation *and* its mobility during low temperature alteration.

Secondly, the isotopic composition of the local mantle and crustal rocks are well constrained, providing reliable end members. The S isotope signature of the mantle immediately beneath the northern Bushveld Complex can be considered to be represented by sulfide inclusions in diamonds within the Klipspringer kimberlite, 25 km east of Mokopane, which exhibit $\delta^{34}S$ values of -1.8 to $+2.4‰$, with a mean of $+1.0‰$ (Westerlund et al., 2004). Previous studies into the isotopic composition of the Transvaal Supergroup have revealed that sulfide-bearing shales from the Duitschland Formation and Timeball Hill Formation have $\delta^{34}S$ signatures ranging from $-18‰$ to $+10‰$ (Cameron, 1982; Sharman-Harris et al., 2005; Sharman et al., 2013). Sulfides within the Duitschland Formation and Malmani Subgroup are isotopically distinct with $\delta^{34}S$ signatures ranging from $+10‰$ to $>+30‰$ (Sharman et al. 3013). Additionally, the abundance of S isotope data available for the adjacent Platreef (Manyeruke et al., 2005;

Fig. 1. Geological map of the northern limb of the Bushveld Complex showing locality of boreholes sampled and farms referred to in the text (adapted from van der Merwe, 2008). Inset map of the entire Bushveld Complex modified from Eales and Cawthorn (1996).

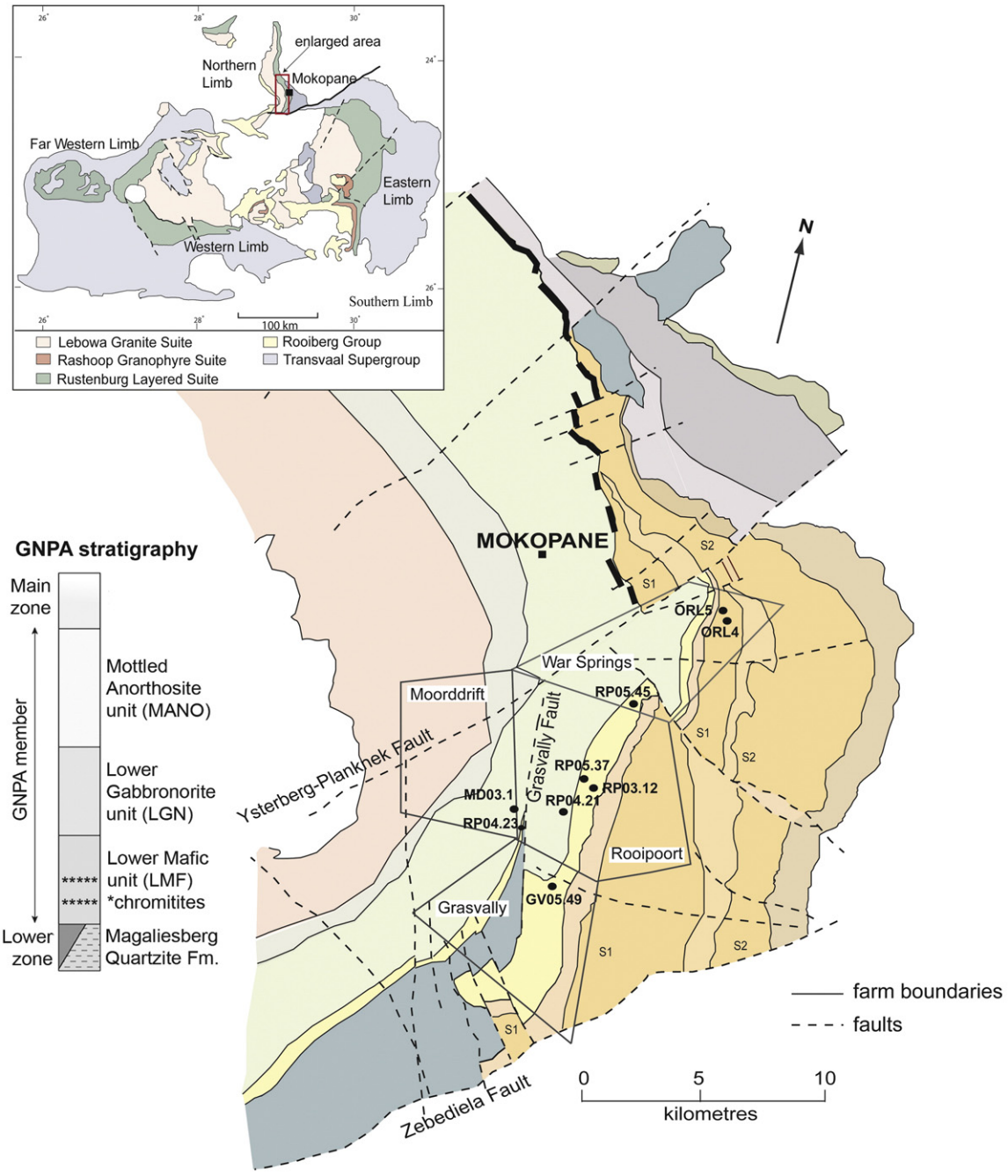

Roof Rocks

Lebowa Granite Suite
Granite, granophyre, leptite, granulite

Rustenburg Layered Suite

Upper Zone
Magnetite gabbro, gabbro, anorthosite, magnetitite

Main Zone
Gabbronorite, gabbro, mottled anorthosite, pyroxenite

GNPA member
Gabbronorite, norite, pyroxenite, chromitite

Platreef
Pyroxenitic lithologies

Lower Zone
Harzburgite, serpentinite, pyroxenite, chromitite

Transvaal Supergroup: Pretoria Group

Magaliesberg Quartzite Fm.

S1 **Silverton Formation**
Carbonaceous shales, limestone

Daspoort Formation
Quartzite

S2 **Strubenskop Formation**
Hornfels, sandy shales

Timeball Hill Formation
Quartzite, shale

Duitschland Formation
Limestone, dolomite, chert, shale

Chuniespoort Group

Malmani Subgroup
Limestone, dolomite, chert

Black Reef Formation
Shale, quartzite

Sharman-Harris et al., 2005; Holwell et al., 2007; Penniston-Dorland et al., 2008) enables a direct comparison of the GNPA member with its nearest analogue. Penniston-Dorland et al. (2012) report $\delta^{34}S$ values for the Merensky Reef and UG2 deposits of $+2.2 \pm 0.6‰$.

There is also S/Se data for other PGE deposits in the Bushveld Complex. Naldrett et al. (2009) report a 'magmatic' S/Se ratio of 2080 for the Merenky Reef, which is lower than the mantle range, though the authors invoke a staging chamber model whereby sulfides partially dissolve prior to emplacement. This would lower the S/Se ratio as explained above by increasing the Se tenor. As such, we do not consider this 'magmatic' range to be representative of the local mantle S/Se signature, but more specific to the Merensky Reef and the processes involved in its formation. In the northern limb, Ihlenfeld and Keays (2011) report a range of S/Se ratios from 1500 to 13,000 for the Platreef which show clear crustal input, but a range of values that extend well below that of the mantle range. McDonald et al. (2012) report S/Se ratios from homogenised sulfide melt inclusions in the Platreef between 400 and 7000, with most in the range 1000-2000. Similarly, this was explained by a process of sulfide dissolution and metal upgrading at depth.

Thirdly, as the GNPA member is underlain by both Lower Zone cumulates and basement metasedimentary rocks the effect, if any, of localised contamination and the in situ assimilation of country rocks along strike should be easily recognized along with any related overprinting signatures.

5. Samples and methods

Samples of quarter core were obtained from nine boreholes drilled by Falconbridge Ltd, Caledonia Mining and Platinum Group Metals on the farm Rooipoort, Grasvally, Moorddrift and War Springs (Fig. 1). The sample suite covers a full range of GNPA member lithological units and mineralized zones, including areas identified by Smith et al. (2011, 2014) that have experienced fluid interaction, and cover a strike length of around 15 km (Fig. 1) that covers footwall consisting of Lower Zone harzburgites, and the Magaliesberg Quartzite Formation (Fig. 1).

The majority of the S isotope data was determined utilizing the in situ laser ablation technique at SUERC within the NERC funded Isotope Community Support Facility (Table 1). This method was favoured over conventional analyses as textural inhomogeneities are easily identifiable, thus enabling the analysis of individual minerals within textually complex multi-phase sulfide aggregates. In addition it also allows analysis of sulfides that would be considered too small for conventional analysis. Polished blocks of 45 samples were placed into a sample chamber, which was evacuated and subsequently filled with an excess of oxygen gas. Sample areas, previously selected using reflected-light microscopy, were combusted using a SPECTRON LASERS 902Q CW Nd-YAG laser (1-W power), operating in TEM00 mode. Details of the system design, laser characteristics and experimental conditions are described in Kelley and Fallick (1990) and Wagner et al. (2002). The SO_2 gas produced by each laser combustion was cryogenically purified in a miniaturized glass extraction line using a CO_2/acetone slush trap to remove water and a standard n-pentane trap to separate SO_2 from trace CO_2. During the laser ablation technique there is a systematic fractionation of $\delta^{34}S$ values of the resulting SO_2 gas compared to the mineral $\delta^{34}S$ (Wagner et al., 2002). The fractionation factors used to correct the data are established for the SUERC facility and are as follows: pyrrhotite +0.4, pentlandite +1.9, chalcopyrite +0.7, pyrite +0.8 and millerite +1.9‰. Repeated analysis of individual sulfide phases revealed in general a reproducibility of ±0.2‰. Larger discrepancies (up to ±1‰) however do exist between and within individual pyrite grains, revealing small-scale heterogeneity. All $\delta^{34}S$ values were calculated relative to the Vienna-Canyon-Diablo Troilite (V-CDT) standard and are reported in standard notation.

Several sulfide samples which exhibited textural and compositional homogeneity in reflected-light were selected for conventional analysis (Table 1). Individual sulfide phases were micro-drilled from nine polished blocks. Each analysis used 4-5 mg of sulfide which was subsequently converted to SO_2 for mass spectrometric analysis by combustion with 0.2 g of cuprous oxide, following the procedure of Robinson and Kusakabe (1975). Samples were combusted under vacuum at 1070 °C for 25 min and the SO_2 gas produced was purified prior to analysis in a VG SIRA II gas mass spectrometer in a glass extraction line analogous to that used for laser analysis. Raw instrument $\delta^{66}SO_2$ data were converted to $\delta^{34}S$ values by calibration with international standards NBS-123 (+17.1‰) and AEA-S-3 (−31.5‰), as well as SUERC's internal lab standard CP-1 (−4.6‰).

Subsequent to $\delta^{34}S$ analysis, Se concentrations of sulfides were determined in-situ by Laser Ablation-ICP-MS using a New Wave Research UP213 UV laser system coupled to a Thermo X Series 2 ICP-MS at Cardiff University. The relative abundances of PGE and other elements were recorded in time-resolved analyses mode (time slices of 250 ms) as the laser beam followed a line designed to sample different sulfide or oxide phases. The beam diameter employed was 30 μm, with a frequency of 10 Hz and a power of ~6 J cm^{-2}. The sample was moved at 6 μm sec^{-1} relative to the laser along a pre-determined line pattern. Ablations were carried out under helium (flow ~0.7 L min^{-1}) and the resulting vapour combined with argon (flow rate 0.65–0.75 L min^{-1}) before delivery to the ICP-MS. Acquisitions lasted between 80 and 400 s, including a 20 s gas blank prior to the start of the analysis and a 10 s washout at the end. Counting errors averaged at 12% and 19% for standards containing 108 ppm Se and 57 ppm Se, respectively.

The S content of sulfides analysed was obtained from a JEOL JXA-8600S electron microprobe at the University of Leicester using an accelerating voltage of 15 kV and a probe current of 30 nA with a focussed beam of <0.5 μm. Sulfur was used as internal standard for the LA work. Subtraction of gas blanks and internal standard corrections were performed using Thermo Plasmalab software. Calibration was performed using a series of 5 synthetic Ni–Fe–S standards prepared from quenched sulfides. The standards incorporate S, Ni, Fe and Cu as major elements and Co, Zn, As, Se, Ru, Rh, Pd, Ag, Cd, Sb, Te, Re, Os, Ir, Pt, Au and Bi as trace elements and the compositions of the 5 standards are given in Prichard et al. (2013).

In order to directly compare in-situ S isotopes with in-situ S/Se ratios, Se concentrations, where possible, were obtained from the same grains as the $\delta^{34}S$ analysis. In samples where the $\delta^{34}S$ analysis resulted in combustion of the entire grain, Se was determined for adjacent grains. In the majority of samples in situ S/Se ratios utilize an average S content of either chalcopyrite, pyrite, pentlandite, pyrrhotite or millerite which were determined by electron microprobe analysis prior to LA-ICP-MS. In samples where microprobe data was not available stoichiometric values of S were used.

Bulk rock S was determined by standard combustion procedures using a Laboratory Equipment Company C2320 (LECO) titrator at the University of Leicester. In total 23 samples were submitted to ALS Global Laboratories, Ireland, for determination of whole rock Se using Aqua Regia digest followed by ICP-MS and ICP-AES.

To recalculate whole rock Pt and Pd contents in 100% sulfide the formula provided by Barnes and Lightfoot (2005) was used:

$$C_{(100\%sul)} = C_{wr} \times 100/(2.527 \times S + 0.3408 \times Cu + 0.4715 \times Ni).$$

where $C_{(100\%sul)}$ is the concentration of Pd or Pt in 100% sulfide, C_{wr} is the concentration of the element in whole rock and *S*, *Cu* and *Ni* is the concentration in wt.% of these elements in whole rock.

A suite of 48 samples of crushed quarter core, representative of the main stratigraphic units of the GNPA member (LMF: 15 samples, LGN: 13 samples and MANO: 20 samples) and the local metasediments (4 samples), were analysed for bulk rock geochemistry as a further indicator of crustal contamination. Major elements were determined by X-ray Fluorescence at the University of Leicester on fusion beads produced by mixing milled powders (ignited to 950 °C to determine loss on ignition) with Johnson-Matthey spectroflux JM100B (80% Lithium Metaborate,

20% Lithium Tetraborate) and then fired in a platinum crucible. Trace elements were determined at Cardiff University using a JY Horiba Ultima 2 inductively coupled plasma optical emission spectrometer (ICP-OES) and Thermo X7 series inductively coupled plasma mass spectrometer (ICP-MS). Ignited powders were fused with Li metaborate on a Claisse Fluxy automated fusion system to produce a melt that could be dissolved in 2% HNO_3 for analysis. Full details of the standard ICP analysis procedures and the instrumental parameters are given in McDonald and Viljoen (2006). Full geochemical data for the suite of samples analysed is given in Table A1 in Appendix A.

6. Sulfur isotopes

The results of more than 130 analyses of sulfides from the GNPA member and associated country rocks are provided in Table 1 and Fig. 2; representing the most comprehensive S isotope study to date on the southernmost sector of the northern limb of the Bushveld Complex. With the exception of the chomitites, the primary and secondary sulfide assemblages are very similar, overlapping the boundary of mantle and crustal values. Our results are in agreement with the limited (n = 16) δ^{34}S data previously presented by Maier et al. (2008) on the GNPA member which ranges from δ^{34}S +1.8‰ to +5.1‰ with a mean of +3.7‰. However, this study did not discriminate between the two important textural and paragenetic generations of sulfide, as our study does.

6.1. Non chromitiferous rocks

6.1.1. Primary sulfide assemblages

The pyrrhotite–pentlandite–chalcopyrite assemblage has a δ^{34}S range of +1.6 to +4‰ with a mean of +2.8‰. Table 1 indicates there is no systematic change with stratigraphic height in any of the drillholes sampled. The majority of analyses reveal signatures indicative of some crustally derived S, with only five analyses, all of which were of pyrrhotite, residing within the local mantle range of −1.8 to +2.4‰ (Table 1). Even where the basal LMF unit is directly underlain by Lower Zone cumulates rather than metasediments of the Transvaal Supergroup, all of the primary sulfides analysed reveal crustal δ^{34}S signatures (Fig. 3A; Table 1).

6.1.2. Secondary sulfide assemblages

The δ^{34}S signatures of 59 analyses of secondary sulfides range from +0.9 to +6.8‰ (mean of +3.5‰; less than 1‰ higher than the mean of the primary sulfides). A crustal S component is evident within the majority of the early pyrrhotite, chalcopyrite and pentlandite although some relicts of primary pyrrhotite and chalcopyrite exhibit δ^{34}S values consistent with local mantle S, but these make up just ten (17%) of the analyses (Table 1). The late pyrite and millerite have δ^{34}S signatures ranging from +2.6 to +6.8‰ (Fig. 3B). Sulfide phases within each sample are fairly consistent in terms of their isotopic composition, with up to 2‰ variation observed (Table 1). There is no evidence of a

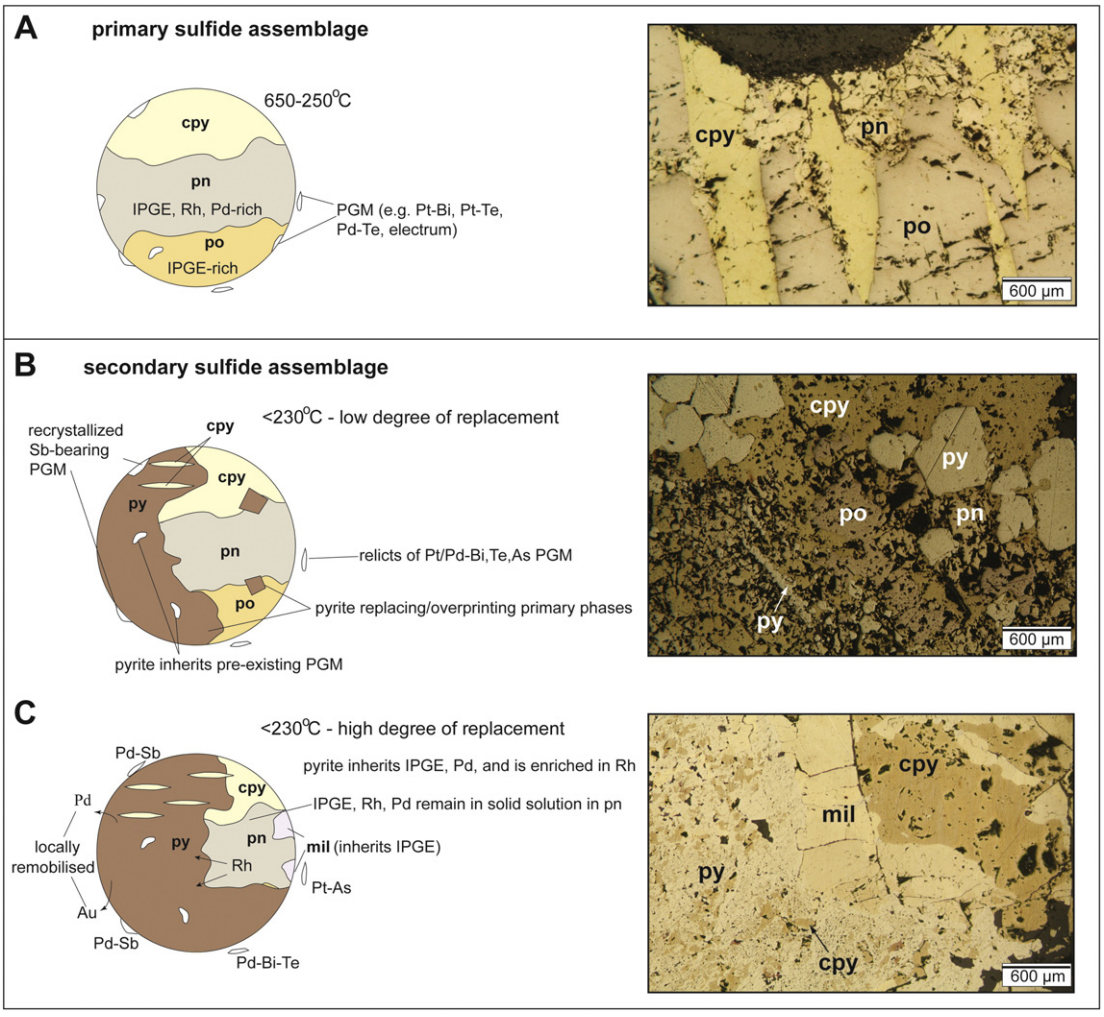

Fig. 2. Summary of the sulfide assemblages observed within the GNPA member showing the key mineralogical and textural changes observed during low temperature alteration of A: a purely magmatic pyrrhotite (pn)-pentlandite (pn)-chalcopyrite (cpy) sulfide assemblage; B and C show variations in the extent of replacement by pyrite (py) and millerite (mil).

Table 1
Results of all conventional (c) and laser (l) S isotope analyses for GNPA member sulfides together with LA-ICP-MS determined S/Se ratios. See Fig. 1 for location of boreholes. Lithological abbreviations: MA mottled anorthosite, PYX pyroxenite, CPX clinopyroxenite, OPX orthopyroxenite, GBN gabbronorite, NR norite, CR chromitite, QTZ quartzite. Sulfide abbreviations cpy chalcopyrite, cub cubanite, po pyrrhotite, pn pentlandite, py pyrite, mil millerite, py* basement pyrite.

Borehole/depth	Lithology	Unit	Sulfide mineral	Sulfide assemblage	$\delta^{34}S$ (‰ VCDT)	Technique	in situ S/Se
RP04.23 — Rooipoort, Lower Zone footwall							
157	MA	MANO	py	s	5.0	l	*2318*
191	PYX	MANO	pn	p	4.0	l	4148
191	PYX	MANO	pn	p	4.0	l	2147
191	PYX	MANO	cpy	p	2.8	l	
201	GBN	LGN	po	s	2.7	l	
305	NR	LMF	po	p	2.8	l	
330	GBN	LMF	po	p	2.0	c	
338	CPX	LMF	po	p	2.9	c	
384	GBN	LMF	po	p	3.5	c	
392	GBN	LMF	po	p	3.4	c	5297
392	GBN	LMF	po	p	3.5	c	4370
392	GBN	LMF	po	p	3.6	l	5335
392	GBN	LMF	cub	p	3.4	l	3289
392	GBN	LMF	cub	p			3156
392	GBN	LMF	cub	p			3466
392	GBN	LMF	pn	p	5.1	l	2613
392	GBN	LMF	pn	p	5.3	l	3621
396	GBN	LMF	po	p	3.3	c	
411	GBN	LMF	po	p	3.1	c	4800
411	GBN	LMF	po	p	3.2	l	2756
411	GBN	LMF	cub	p	4.0	l	*4083*
411	GBN	LMF	pn	p	5.0	l	*4136*
RP05.45 — Rooipoort, quartzite footwall							
146	GBN	LMF	py	s	6.8	l	*3764*
149	GBN	LMF	mil	s	3.9	l	
149	GBN	LMF	mil	s	3.6	l	
149	GBN	LMF	py	s	5.0	l	
149	GBN	LMF	py	s	4.2	l	
149	GBN	LMF	cpy	s	4.7	l	
165	GBN	LMF	cub	s	4.1	l	3535
165	GBN	LMF	cub	s	3.9	l	4776
165	GBN	LMF	py	s	3.9	l	4180
165	GBN	LMF	py	s	4.9	l	8267
165	GBN	LMF	py	s	4.9		4233
165	GBN	LMF	py	s		l	3948
165	GBN	LMF	mill	s	4.9	l	
166	CR	LMF	py	s	6.9	c	8611
166	CR	LMF	py	s	5.8	l	8546
166	CR	LMF	cub	s	5.3	l	5146
166	CR	LMF	cub	s			4116
166	CR	LMF	mil	s			*2305*
167*	CR	LMF	py	s	6.6	l	>8915 (min value as Se BDL)
167	CR	LMF	py	s	6.1	l	3364
167	CR	LMF	py	s	6.9	l	5183
167	CR	LMF	py	s	7.1	l	4863
167	CR	LMF	cub	s	5.4	l	1877
167	CR	LMF	cub	s	6.1	l	4096
167	CR	LMF	cub	s	4.4	l	4412
167	CR	LMF	cpy	s	4.4	l	
167	CR	LMF	cpy	s	2.8	l	
167	CR	LMF	pn	s	5.4	l	1919
167	CR	LMF	pn	s	5.6	l	2662
167	CR	LMF	pn	s	7.5	l	3015
167	CR	LMF	mill	s			*2420*
205	NR	LMF	py	s	4.1	l	
205	NR	LMF	py	s	4.3	l	
205	NR	LMF	mil	s	4.1	l	
205	NR	LMF	cpy	s	3.8	l	
206	CPX	LMF	cpy	s	3.9	l	
208	NR	LMF	py	s	5.0	l	8829
208	NR	LMF	py	s	4.9	l	*3047*
208	NR	LMF	py	s			*5612*
208	NR	LMF	pn	s	6.0	l	3695
208	NR	LMF	pn	s	5.8	l	2035
208	NR	LMF	pn	s			*2325*
208	NR	LMF	cub	s	5	l	*2134*
212	QTZ	FLR	py *	b	4.5	l	
212	QTZ	FLR	py *	b	4.1	l	
214	QTZ	FLR	py *	b	5.3	l	7731
214	QTZ	FLR	py *	b	5.6	l	*8441*

Table 1 (*continued*)

Borehole/depth	Lithology	Unit	Sulfide mineral	Sulfide assemblage	$\delta^{34}S$ (‰ VCDT)	Technique	in situ S/Se
RP05.45 — Rooipoort, quartzite footwall							
214	QTZ	FLR	py *	b	6.2	l	6916
214	QTZ	FLR	cub	s	3.6	l	3052
214	QTZ	FLR	cub	s	4.1	l	5917
214	QTZ	FLR	cub	s	4.5	l	
214	QTZ	FLR	mil	s	5.6	l	*2217*
214	QTZ	FLR	py	s	4.3	l	6476
215	QTZ	FLR	py *	b	4.1	c	6693
215	QTZ	FLR	py *	b	3.5	c	7875
215	QTZ	FLR	py *	b			5943
RP04.21 — Rooipoort, quartzite footwall							
448	MA	MANO	cpy	s	3.5	l	
448	MA	MANO	py	s	4.1	l	
448	MA	MANO	py + mil	s	3.6	l	
460	MA	MANO	po	p	2.3	l	
460	MA	MANO	po	p	2.5	l	
679	MA	MANO	py	s	3.5	l	8980
679	MA	MANO	py	s	3.0	l	3619
679	MA	MANO	py	s			*5693*
679	MA	MANO	po	s	1.7	l	2797
679	MA	MANO	po	s			3494
679	MA	MANO	po	s			*2802*
679	MA	MANO	pn	s	3.2	l	2126
679	MA	MANO	pn	s			2517
679	MA	MANO	cub	s	1.3	l	3328
679	MA	MANO	cub	s			2709
681	MA	MANO	cpy	s	2.8	l	
681	MA	MANO	pn + mil	s	2.4	l	
690	GBN	MANO	po	p	1.6	l	3564
690	GBN	MANO	po	p	1.9	l	3391
690	GBN	MANO	po	p	1.8	l	2592
690	GBN	MANO	po	p	2.9	l	3562
690	GBN	MANO	pn	p			*2941*
690	GBN	MANO	cpy	p			*4004*
693	GBN	MANO	po	p	2.6	l	4409
693	GBN	MANO	po	p	3.1	l	3922
693	GBN	MANO	po	p			3456
693	GBN	MANO	pn	p	4.0	l	2032
693	GBN	MANO	pn	p	4.7	l	3680
693	GBN	MANO	cpy	p	3.3	l	*4008*
MD03.1 — Moorddrift, Lower Zone footwall							
552	OPX	MANO	pn	s	3.5	l	*2106*
552	OPX	MANO	cub	s	2.4	l	2961
552	OPX	MANO	cub	s	2.9	l	2272
542	QTZ vein	MANO	cpy	s	8.1	c	
542	QTZ vein	MANO	cpy	s	8.0	c	
573	fracture fill	MANO	cpy	s	11.4	c	
573	fracture fill	MANO	cpy	s	11.9	c	
RP05.37 — Rooipoort, quartzite footwall							
106	GBN	MANO	py	s	4.0	l	
RP03.12 — Rooipoort, quartzite footwall							
140	GBN	LMF	py	s	2.3	l	
140	GBN	LMF	py	s	3.6	l	
144	PYX	LMF	py	s	4.5	l	
145	Cr	LMF	py	s	4.8	l	
GV05.49 — Grasvally, quartzite footwall							
127	Cr	LMF	py	s	4.3	l	
127	Cr	LMF	cpy	s	3.6	l	
128	Cr	LMF	py	s	6.3	l	
128	Cr	LMF	cpy	s	5.7	l	
128	Cr	LMF	pn	s	5.1	l	
140	GBN	LMF	po	s	4.0	l	
140	GBN	LMF	po	s	4.7	l	
140	GBN	LMF	cpy	s	3.2	l	
140	GBN	LMF	py	s	3.6	l	
214	QTZ	FLR	py*	b	10.5	l	
214	QTZ	FLR	py*	b	9.8	l	
ORL 4 — War Springs, quartzite footwall							
65	MA	MANO	py	s	3.5	l	
65	MA	MANO	pn	s	3.8	l	
65	MA	MANO	cpy	s	2.9	l	

(*continued on next page*)

Table 1 (*continued*)

Borehole/depth	Lithology	Unit	Sulfide mineral	Sulfide assemblage	δ^{34}S (‰ VCDT)	Technique	in situ S/Se
ORL 4 — War Springs, quartzite footwall							
221	PYX	LMF	cpy	s	1.9	l	
221	PYX	LMF	py	s	2.6	l	
221	PYX	LMF	py	s	2.4	l	
221	PYX	LMF	po	s	1.9	l	
221	PYX	LMF	po	s	0.9	l	
395	PYX	LMF	po	s	3.7	l	
395	PYX	LMF	po	s	4.2	l	
395	PYX	LMF	py	s	2.6	l	
395	PYX	LMF	pn	s	4.2	l	
606	CR	LMF	po	s	5.5	l	
606	CR	LMF	po	s	5.3	l	
606	CR	LMF	po	s	5.8	l	
606	CR	LMF	po	s	5.3	l	
606	CR	LMF	cpy	s	5.1	l	
606	CR	LMF	cpy	s	5.9	l	
606	CR	LMF	po	s	4.6	l	
ORL5 — War Springs, quartzite footwall							
97	MA	MANO	py	s	3.2	l	
97	MA	MANO	py	s	3.2	l	
108	GBN	LMF	py	s	2.6	l	
108	GBN	LMF	cpy	s	2.6	l	
597	PYX	LMF	py	s	5.1	l	
597	PYX	LMF	py	s	5.0	l	
597	PYX	LMF	pn	s	5.8	l	

S/Se ratios that are in italics represent the mean of several mineral analyses with comparable/Se ratios.

stratigraphic or lateral control over the distribution/preservation of the mantle like signatures as they are distributed throughout the GNPA member irrespective of a Lower Zone cumulates or quartzite footwall.

6.2. Chromitiferous rocks

Throughout the GNPA, the chromitites in the LMF are isotopically distinct from the rest of the GNPA member, with δ^{34}S values consistently 1 to 2‰ heavier than the primary and secondary sulfide assemblages (see Fig. 3C), ranging from +2.8 to +7.1‰ with a mean of +5.4‰ (Table 1; Fig. 3C).

6.3. Country rocks

Sulfides within the quartzite footwall, interpreted to have resulted from infiltration of the magmatic sulfide liquid into the footwall (Smith et al., 2011) and are thus fundamentally magmatic, are isotopically similar to those developed within the GNPA member, exhibiting a range from δ^{34}S +3.6 to +5.6‰ (Table 1; chalcopyrite and millerite, Fig. 3D). Conversely, metasedimentary pyrite hosted within the Magaliesberg Quartzite Formation displays greater variation in δ^{34}S signatures and a very strong crustal component with values ranging from δ^{34}S +3.5 to +10.5‰ (Table 1; basement pyrite, Fig. 3D).

7. Bulk rock S/Se ratios

Rocks with visible sulfide mineralization in the GNPA member typically contain 0.1 to 2 wt.% S and Se concentrations of <0.2 (detection limit) to 6.1 ppm (Table 2). Due to the highly compatible nature of Se in sulfide a strong positive correlation exists between S and Se throughout the succession (Fig. 4A). Sulfur/selenium ratios are variable from 1495 to 6765, with the majority of samples residing within or below the mantle range of Eckstrand and Hulbert (1987); Table 2; Fig. 4A). However, a few samples exhibited ratios that exceed that of the mantle (Fig. 4A; Table 1), thus being consistent with a crustal source of at least some of their S. All these are from samples from the LMF unit, most of which were obtained west of the Grasvally Fault where Lower Zone cumulates underlie the GNPA member (Table 2). The footwall quartzite samples straddle the upper boundary of the mantle range, however, these samples contain both metasedimentary pyrite and also some magmatically-derived sulfide and so represent a mixed signature.

From the broad negative correlation observed between PGE tenor (defined by Pt + Pt in 100% sulfide) and S/Se ratio, primary and secondary sulfides can be distinguished (Fig. 4B). The former are, in general, characterized by relatively low PGE tenors (typically between 6 and <60 ppm, with the exception of the chromitite; Table 2), and S/Se ratios within or above the mantle range (3500–6500; Table 2). In comparison, secondary sulfides are characterized by notably lower S/Se ratios from 1495 to 4210 with only two samples residing within the crustal field, and generally higher PGE tenors (40 to <160 ppm Fig. 4B; Table 2). Fig. 4B illustrates clearly that as the S/Se ratio decreases, the PGE tenor progressively increases, signifying either S-loss or addition of Se and PGE. The Se content throughout the GNPA member increases relative to bulk PGE content (Table 2), indicating that both are controlled relatively analogously by the presence of sulfide. A strong correlation also exists between PGE tenor and Se tenor throughout primary and secondary sulfides (Fig. 5).

8. Mineral-scale S/Se ratios

8.1. The Se content of sulfide minerals

The Se contents of pyrrhotite, chalcopyrite, pentlandite, millerite and pyrite typically varies from the detection limit of 60 ppm up to 170 ppm (Table 3). Within the chromitites, concentrations of Se are noticeably elevated with pentlandite and millerite containing up to 220 ppm and 600 ppm, respectively. Representative time resolved analysis (TRA) spectra for the major sulfide phases analysed are provided in Fig. 6. Although the Se content of the individual sulfide phases varies slightly between samples, Se appears to be distributed uniformly within each sulfide phase, as shown by the smooth profiles on the TRA spectra that mirror S (Fig. 6). This clear relationship along the laser lines, plus multiple analyses from single grains indicates a precision within 10%. While all the magmatic sulfide phases contain detectable concentrations of Se in solid solution (Fig. 6A–G), the Se contents of metasedimentary pyrite in the local footwall is noticeably lower at <68 ppm (Fig. 6H).

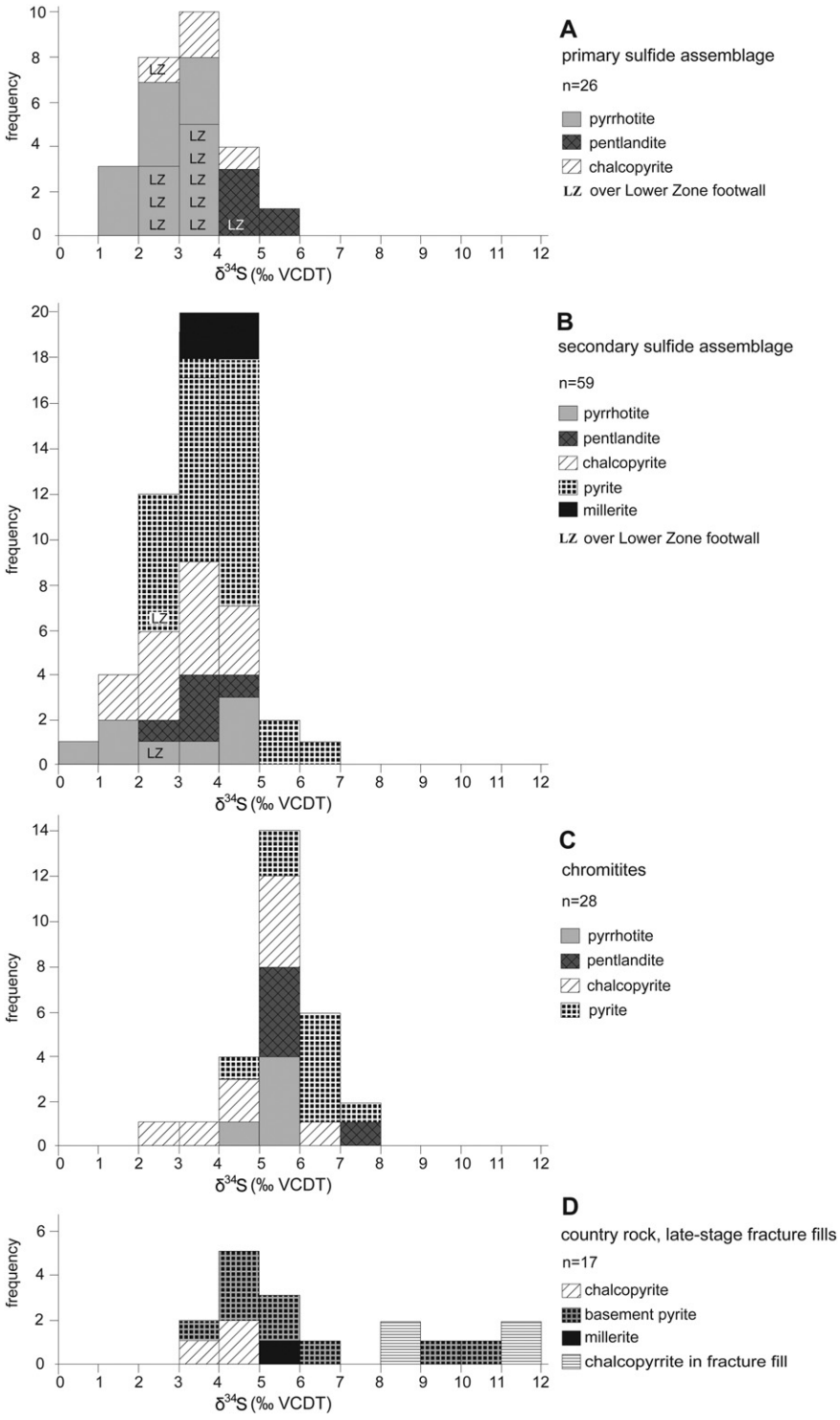

Fig. 3. Range in δ34S values for all observed sulfide phases within the GNPA member and its footwall for A: primary sulfide assemblage; B: secondary sulfide assemblage; C: sulfides developed within chromitites; and D: sulfides present within the local footwall and late-stage fracture fills. LZ indicates samples analysed with a Lower Zone footwall.

8.2. The S/Se ratios of sulfide minerals

The S/Se ratio of sulfides was calculated using Se concentrations from LA-ICP-MS analysis and S contents determined by electron microprobe. The S values represent averages of the sulfide phase in each sample. Where microprobe data was not available, stoichiometric S values were utilized. The results are shown in Fig. 7. Sulfur/selenium ratios in the primary chalcopyrite, pyrrhotite and pentlandite vary from 2032 to 5726 (Fig. 7A). Mantle-like S/Se ratios are widespread and are observed in all sulfide phases. Only a few pyrrhotite analyses from west of the Grasvally Fault exhibit S/Se ratios below mantle.

In the secondary assemblages, any relicts of primary pyrrhotite, chalcopyrite and pentlandite show a range in ratios of 2035 to 5917; almost identical to the primary sulfide assemblages although most occurrences fall within the range of 2035 to 3695, which includes a significant proportion of pentlandite displaying S/Se ratios lower than mantle

Table 2
Whole rock S and Se for primary (p) and secondary (s) sulfide-bearing samples within the GNPA member together with PGE tenors (calculated using Barnes and Lightfoot, 2005 formula). Abbreviations FLR floor rocks (quartzites), LMF Lower Mafic Unit, MANO Mottled Anorthosite Unit and CR chromitite.

Borehole	Sample/ depth	Unit	Sulfide type primary/secondary	Se (ppm)	S wt.%	S/Se	Pt + Pd (ppb)	Pd in 100% sulfide (ppm)	Pt + Pd in 100% sulfide (ppm)
RP04.23	144	MANO	p	6.10	2.108	3456	1168	17	20
	157	MANO	s	3.00	0.806	2686	932	38	43
	201*	MANO	s	<0.20	0.084	4210*	143	41	61
	300	CR	p	1.50	0.266	1773	978	40	127
	305	LMF	p	3.50	0.751	2145	129	4	6
	338	LMF	p	0.70	0.292	4175	281	9	36
	384	LMF	p	0.70	0.406	5804	167	12	15
	392	LMF	p	0.90	0.512	5692	161	8	11
	411	LMF	p	0.70	0.434	6195	85	5	7
RP05.45	146	LMF	s	0.40	0.123	3067	139	34	49
	165	LMF	s	0.20	0.135	6765	126	27	36
	167	CR	s	2.10	0.735	3500	3603	85	153
	205	LMF	s	2.50	0.374	1494	1454	132	154
	208	LMF	s	0.50	0.080	1596	520	157	231
	215	FLR	s	1.20	0.428	3566	760	50	61
	214	FLR	s	8.30	3.340	4024	3389	26	36
RP04.21	448	MANO	s	1.00	0.379	3786	1064	70	103
	681	MANO	s	0.90	0.368	4083	474	33	48
	690	MANO	p	4.40	1.650	3750	1283	23	29
	693	MANO	p	2.00	0.808	4038	1048	31	48
MD03.1	552	MANO	s	4.70	0.991	2108	1915	32	66
GV02.1	166	MANO	p	3.90	1.468	3765	2115	46	56
	476	LMF	s	3.20	1.856	5800	675	7	13

201* S/Se ratio is a minimum value as detection limit is 0.2 for Se.

(Fig. 7B; Table 1). Secondary pyrite and millerite, including those within the chromitites are characterised by more variable S/Se ratios which fall within the range of 1975 to 8980 (Table 1). Pyrite from the quartzite footwall exhibits unequivocally crustal S/Se ratios in the crustal range of 5943–8455 (Fig. 7B; Table 1).

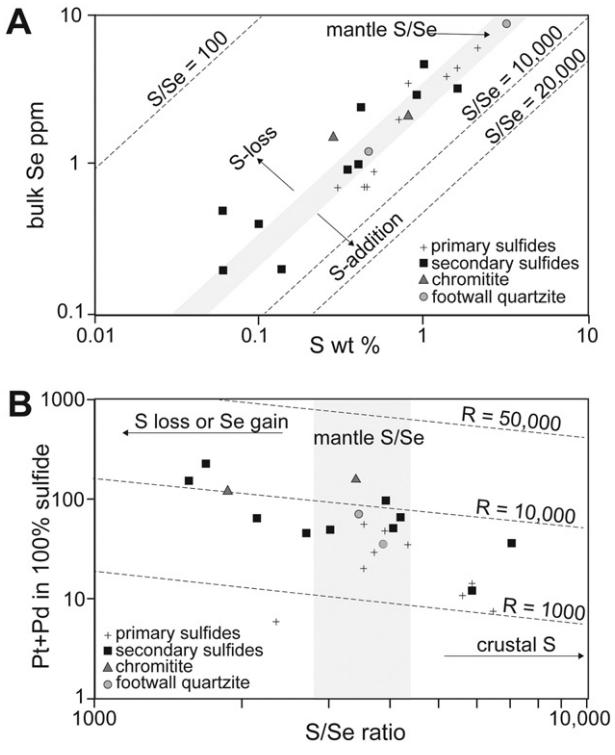

Fig. 4. A Sulfur in wt% versus Se (ppm) for different sulfide assemblages hosted within the GNPA member. B. PGE tenor (Pt + Pd in 100% sulfide), versus bulk S/Se ratio for samples within the GNPA member. Mantle S/Se range is taken from Eckstrand and Hulbert (1987). Data is overlain by different R-factor values which are taken from Queffurus and Barnes (2015).

9. Trace element indicators of crustal contamination

While S isotopes and S/Se ratios are used to determine crustal contamination specifically involving the addition of S, a number of trace element ratios can reveal more general crustal contamination signatures. Therefore, we also include an analysis of trace element data to further investigate the role of contamination, and independently test the apparent contamination signatures shown by the S/Se ratios and S isotopes. Chondrite-normalized rare earth element (REE) patterns for the GNPA member and its local footwall are provided in Fig. 8A–F, with the data included as Table A1 in Appendix A. Overall the LMF, LGN and MANO units are characterised by: (i) relatively fractionated REE patterns (La/Lu_n 1.6–14), enriched in the light rare earth elements (LREE); (ii) almost no fractionation of the HREE (Tb/Yb_n 1.1); and (iii) a mostly positive Eu anomaly (Eu/Eu^* 0.8–3.6). The most fractionated profiles (La/Lu_n 5–12) within the GNPA member are associated with samples obtained from the MANO and LMF units overlying metasediments (Fig. 8A, B). Here the rocks show strong enrichment in LREE (Ce/Sm_n 2.1–3.6) and almost no fractionation of the HREE (Tb/Yb_n ~ 1).

It is worth noting that the individual profiles of samples from borehole RP05.45 do not necessarily become progressively enriched in REE with depth (Table A1 in Appendix A) and thus proximity to the quartzite footwall. However, LREE concentrations are noticeably elevated

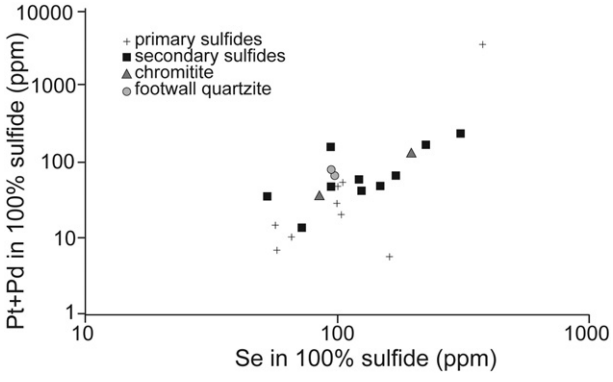

Fig. 5. Relationship between Pt + Pd tenor and Se tenor.

Table 3
Average LA-ICP-MS determined Se concentrations of pyrrhotite, pentlandite and chalcopyrite/cubanite in primary and secondary sulfide assemblages, together with low temperature pyrite and millerite. To reduce the error associated with the ratios all values <80 ppm have been excluded. Note the detection limit for Se is 60 ppm. An indication of the analytical error is propagated from using the average 12% counting variation observed on the in house Cardiff standard which contains 108 ppm Se.

	Se concentration in ppm										
Sample	po	pn	cpy/cub	py	mil	po:pn	po:cpy	pn:cpy	py:pn	py:cpy	py:mil
RP04.23/392											
Min		92	102								
Max	88	128	112								
Mean	88	110	107			0.8 ± 0.1	0.8 ± 0.1	1.0 ± 0.1			
Error	11	13	13								
n	1	2	3								
RP04.23/411											
Min	80		85								
Max	139	83	89								
Mean	109	83	87			1.3 ± 0.2	1.3 ± 0.2	1.0 ± 0.1			
Error	13	10	10								
n	2	2	2								
RP04.21/690											
Min	97	103	86								
Max	161	127	91								
Mean	114	115	89			1.0 ± 0.1	1.3 ± 0.2	1.3 ± 0.2			
Error	14	14	11								
n	11	3	2								
RP04.21/679											
Min	108	109	107	110							
Max	140	156	131	148							
Mean	129	135	119	135		1.0 ± 0.1	1.1 ± 0.1	1.1 ± 0.2	1.0 ± 0.1	1.1 ± 0.2	
Error	16	16	14	16							
n	5	5	2	3							
RP04.21/693											
Min	85	90									
Max	109	164									
Mean	97	127				0.8 ± 0.1					
Error	12	15									
n	3	2									
RP05.45/165											
Min				128							
Max			100	137							
Mean			100	131						1.3 ± 0.2	
Error			12	16							
n			1	3							
RP05.45/166-chromitite											
Min					152						
Max					593						
Mean		214	85		345			2.5 ± 0.2			
Error		26	10		41						
n		1	1		4						
RP05.45/167-chromitite											
Min		103	84	103	134						
Max		173	183	159	162						
Mean		127	134	125	148			1.0 ± 0.1	1.0 ± 0.1	0.9 ± 0.1	0.8 ± 0.1
Error		15	16	15	18						
n		4	2	5	2						
RP05.45/208											
Min		91		106							
Max		164		229							
Mean		140	121	165	131			1.2 ± 0.2	1.2 ± 0.2	1.4 ± 0.2	1.3 ± 0.2
Error		17	15	20	16						
n		8	1	8	1						
RP05.45/214											
Min					153						
Max					166						
Mean			116		159						
Error			14		19						
n			1		2						
MD03.1/552											
Min		120	161								
Max		156	155								
Mean		138	158					0.9 ± 0.1			
Error		17	19								
n		2	2								

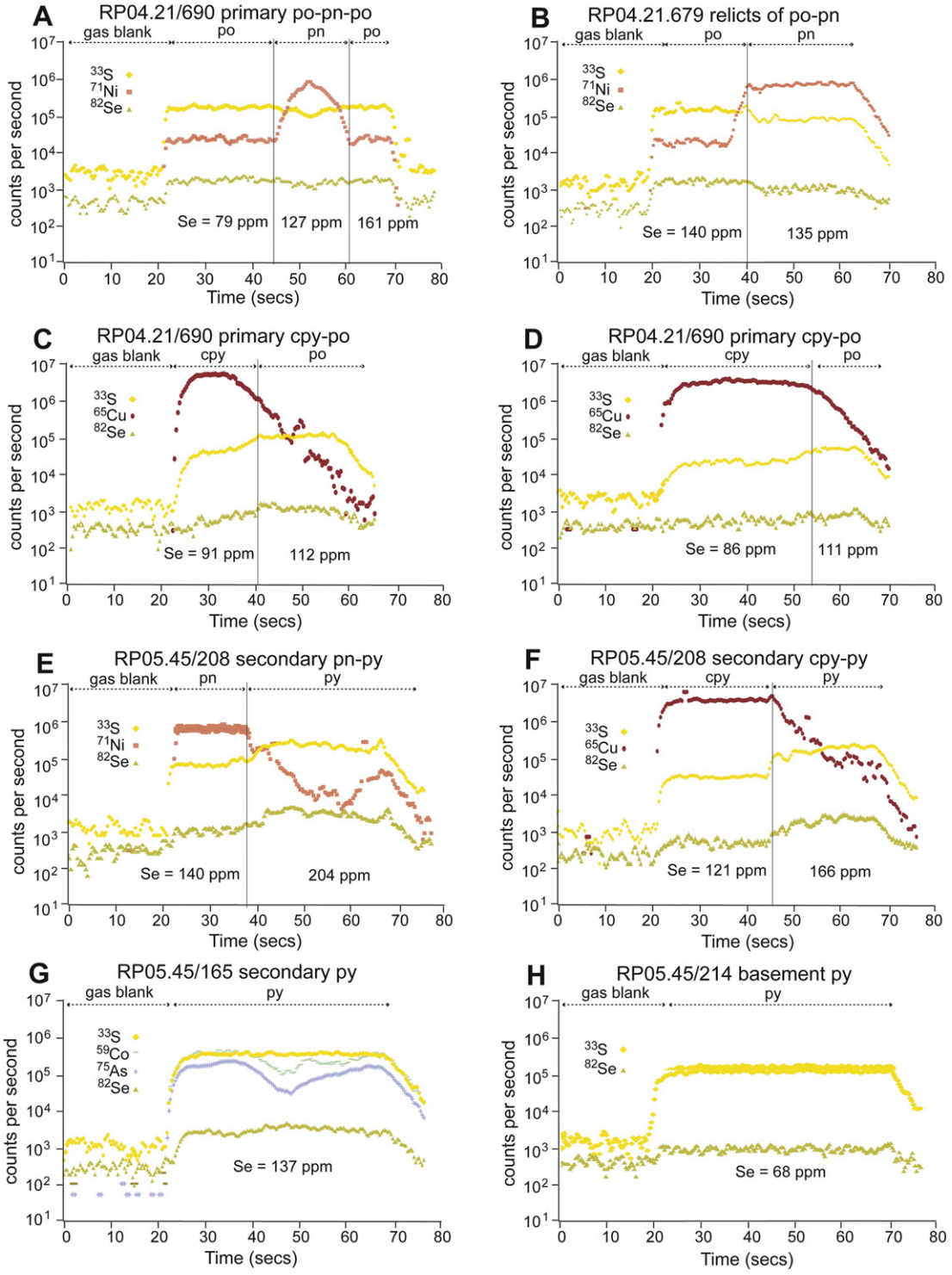

Fig. 6. Selected LA-ICP-MS TRA spectra for A and B: primary pyrrhotite and pentlandite; C and D: primary chalcopyrite and pyrrhotite; E: pyrite replacing pentlandite; F: pyrite and chalcopyrite relicts; G: secondary pyrite developed within the GNPA member zoned in Co and As; and H: pyrite from the Magaliesberg Quartzite Formation.

within the LMF unit that overlies quartzite (Fig. 8B, c.f. Fig. 8D), indicating some localised contamination over the quartzites. The quartzites themselves exhibit highly fractionated REE patterns (La/Lu_n 11–19) that are significantly more enriched than those of the GNPA lithologies (Fig. 8F).

In contrast, where Lower Zone cumulates underlie the GNPA member, REE concentrations are comparable between the LMF and MANO units (Fig. 8D, E). Here, REE profiles are fractionated and LREE enriched but less so than observed where the floor is quartzite. Most LMF samples show lower La/Lu_n (1.6–4.8) and Ce/Sm_n (1.3–2) ratios. The LGN unit is notably homogeneous in its REE contents and geochemistry in comparison to the overlying MANO unit and underlying LMF unit, (Fig. 8C) and are consistent with Main Zone data from the Western Bushveld (Maier and Barnes, 1998), and the interpretation this is a sill of Main Zone (de Klerk, 2005; Maier et al., 2008; Smith et al., 2014).

Primitive mantle-normalized, multi-element spider diagrams of representative samples from the GNPA member and its local quartzite footwall are presented in Fig. 9. Throughout the succession, trace element

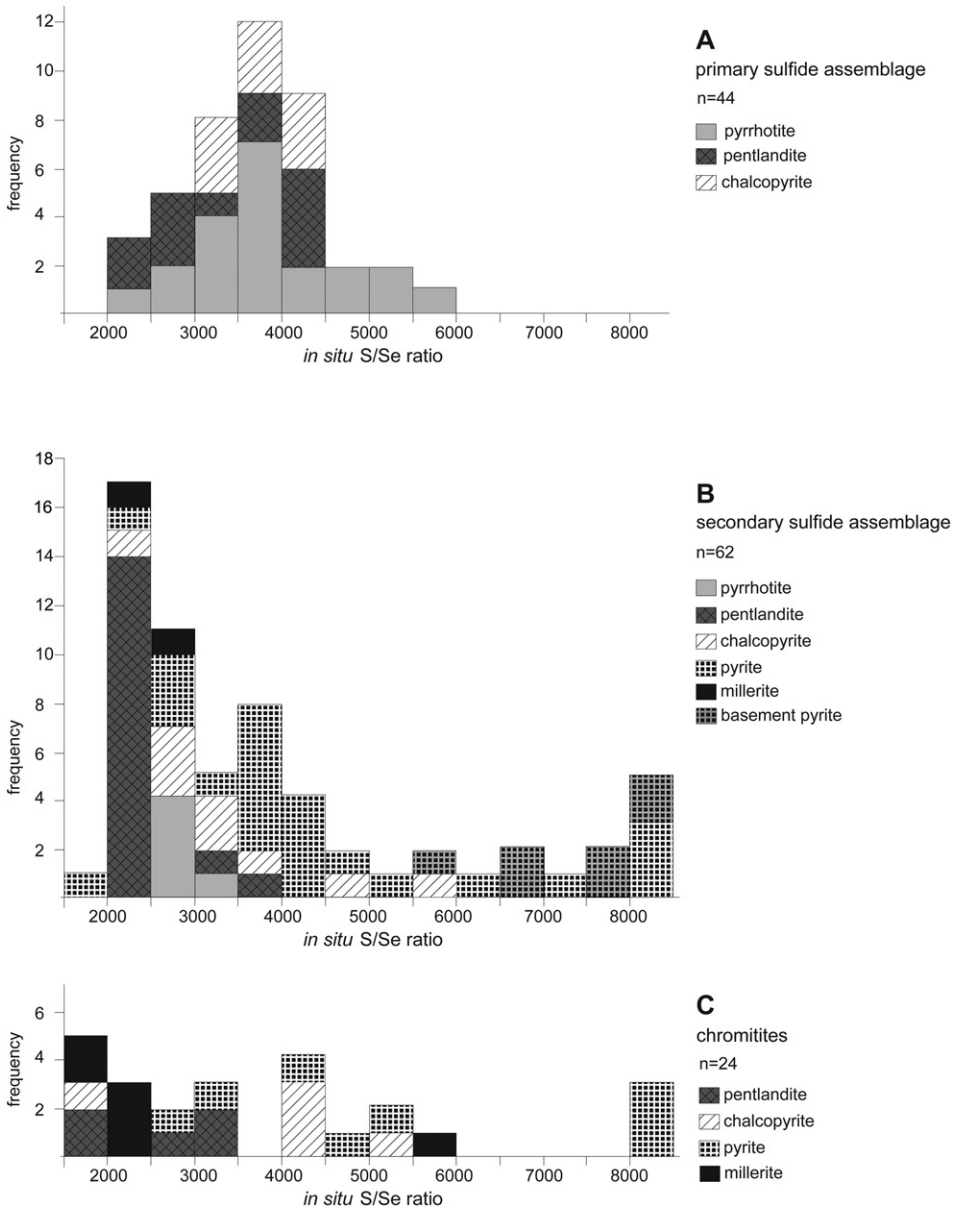

Fig. 7. Range in S/Se ratio for individual sulfide phases calculated from LA-ICP-MS for A: primary sulfide assemblage; B: secondary sulfide assemblage; C: sulfides developed within chromitites.

signatures are consistent and characterised by pronounced negative Nb, Sr and Ti anomalies and strong enrichment in LILE; all strong indicators of crustal contamination. While the MANO and LMF units exhibit variations in absolute trace element concentrations (Fig. 9A, C), the LGN unit exhibits an extremely restricted range in its trace element content and geochemistry (Fig. 9B).

The majority of GNPA samples exhibit low $(Nb/Th)_{PM}$ ratios (<0.4) and elevated $(Th/Yb)_{PM}$ ratios (1–24), thus defining a relatively tight trend (very similar to that observed in the Platreef; Ihlenfeld and Keays, 2011) on the $(Nb/Th)_{PM}$ vs. $(Th/Yb)_{PM}$ plot in Fig. 9. With $(Nb/Th)_{PM}$ ratios <1 and $(Th/Yb)_{PM}$ ratios >5 considered indicative of a crustally contaminated mantle derived magma (Lightfoot and Hawkesworth, 1988; Lightfoot et al., 1990; Ihlenfeld and Keays, 2011), a crustal influence is noticeable throughout the GNPA member with only a few samples residing within the purely magmatic range (Fig. 10). From the data shown in Figs. 9 and 10 however, it is evident that the degree of contamination is not a function of proximity to local footwall metasediments as the basal LMF unit exhibits a similar range in $(Nb/Th)_{PM}$ and $(Th/Yb)_{PM}$ ratios to the LGN and MANO units, with this data indicating a signature of bulk contamination of the entire package, and the REE data showing evidence of some localised contamination in addition.

10. Discussion

10.1. Comparison of S isotopes and S/Se ratios

Fig. 11 compares the S isotope data with the bulk rock S/Se data and illustrates that for individual samples, the $\delta^{34}S$ signatures are rarely in agreement with the S/Se ratios in terms of mantle versus crustal signatures. The notable lack of relationship between bulk rock S/Se ratios and S isotopes within the GNPA member is particularly apparent within the chromitites, which exhibit the most crustal $\delta^{34}S$ signatures but are characterized by consistently mantle-like S/Se ratios (Fig. 11). This clearly shows that a simple assessment of either of these alone cannot be used with confidence to interpret the source of S unambiguously.

One particularly interesting relationship our data show is that during secondary alteration, there is a trend for S/Se ratios to lower to

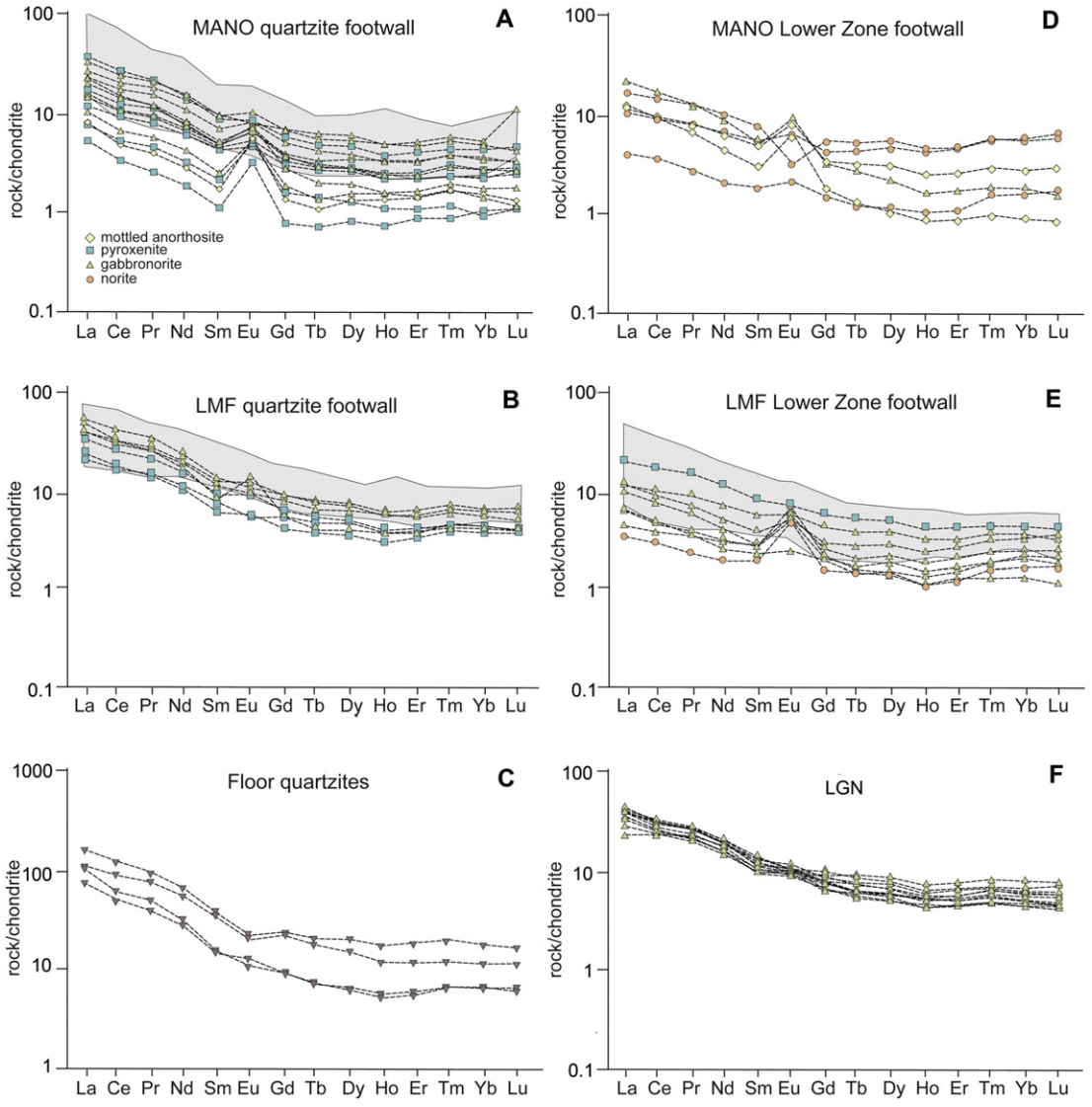

Fig. 8. Chondrite normalized rare earth element plots for A: the mottled anorthosite unit where underlain by quartzites, B: the Lower Mafic unit where underlain by quartzites, C: footwall quartzites from the Magaliesberg Quartzite Formation (note the different scale on the y axis), D: the mottled anorthosite unit where underlain by Lower Zone, E: the Lower Mafic unit where underlain by Lower Zone, and F: the Lower Gabbronorite unit. Shaded fields on A, B and E represent data from Maier et al. (2008).

mantle values or below, whereas S isotope values rise to more crustal values (Figs. 3, 11). This apparent paradox illustrates the inherent problem in using these ratios as purely crustal contamination indicators. The overall shift of just under 1‰ in $\delta^{34}S$ signatures to heavier values in the secondary sulfide assemblages could very easily be explained by the addition of crustal S during secondary alteration. However, this should also increase the S/Se ratio, which it does not. In fact, the reduction in S/Se ratio in the secondary assemblages is more indicative of S loss, rather than gain, which is highly likely a consequence of the secondary sulfide alteration. The increase in PGE tenor along with the reduction in S/Se (increase in Se tenor; Fig. 4) supports this. Given the mineralogical and geochemical work of Smith et al. (2011, 2014), it is unlikely the secondary alteration introduced any further PGE, and so the increase in tenor during alteration is most likely due to S-loss. Naldrett et al. (2009) also note high PGE tenors and a very consistent, low S/Se ratio of 2080 in the Merensky Reef. They interpret the high tenors to be due to sulfide dissolution in a staging chamber, and while this is a different process to the low temperature alteration, the result of losing S relative to Se and PGE is the same.

As such, our work this shows how secondary processes can mask the crustal signatures in S/Se ratios. While it is possible that crustal S was added during this process to raise the S isotope signatures, there would still have to be a large net S loss. What is more likely is that this small shift in S isotope compositions is a result of this alteration. Crystallization of pyrite at low temperatures (<250 °C) fractionates $\delta^{34}S$ by around +1.5‰ (Ohmoto and Rye, 1979), which would explain perfectly how the pyrite-dominant secondary sulfide assemblage appears around 1‰ heavier than the primary assemblages, without the need to add S in the process.

10.2. Comparison of bulk and mineral S/Se ratios

Fig. 12 compares the bulk rock S/Se ratios to those of individual sulfide minerals within each sample. The in situ S/Se ratios show a very high variability and complexity in comparison to bulk rock ratios (Fig. 12), and in some cases, all our individual analyses sit below or above the bulk rock value, showing that they cannot be fully representative of the overall sulfide population within the sample. This may reflect that in 3D, there are more than one type of sulfide assemblage (primary v secondary) than exposed in the surface of a 2D section. For example, the bulk rock S/Se value for the basement quartzite sample (RP05.45/214) sits within the mantle range. However, the rock is

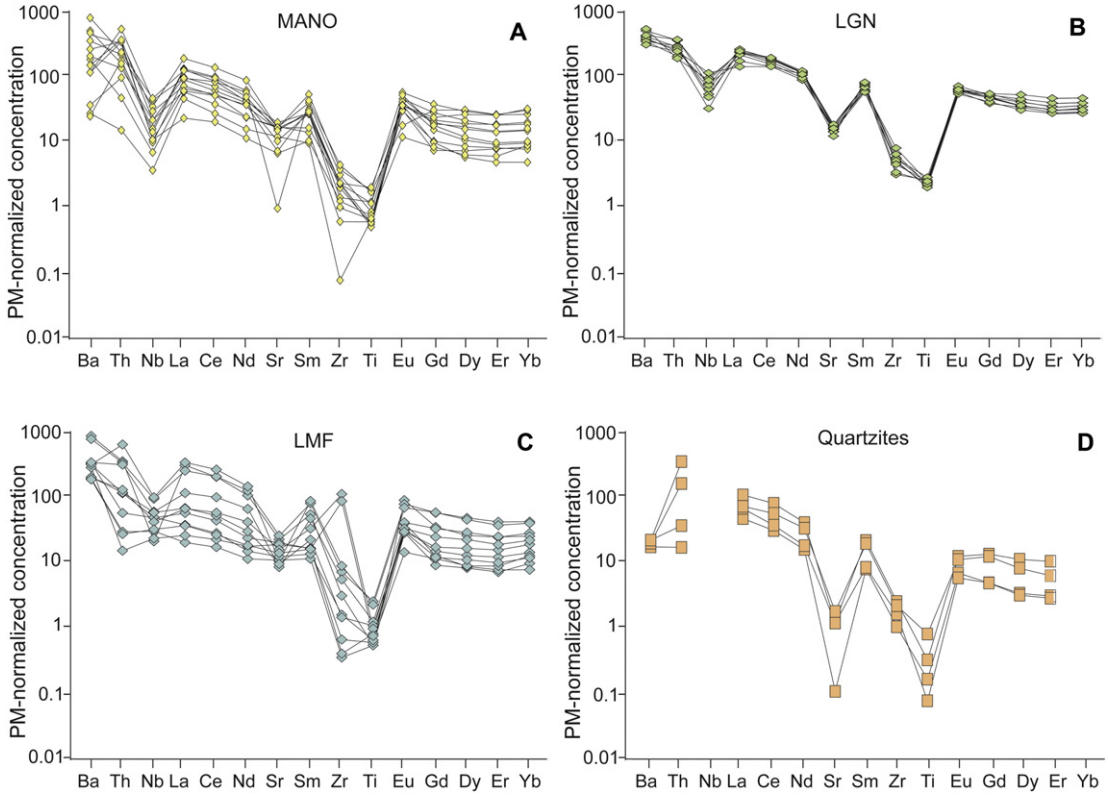

Fig. 9. Primitive mantle-normalized trace element patterns for samples for A: the Mottled Anorthosite unit (MANO), B: the Lower Gabbronorite unit (LGN), C: the Lower Mafic unit (LMF), and D: quartzites from the Magaliesberg Quartzite Formation.

known to contain sulfides of two different generations: sulfides that have infiltrated the floor from the GNPA member, such as pentlandite, have low S/Se ratios; whereas the metasedimentary pyrites have high S/Se ratios around 7000–9000 (Fig. 12B). This illustrates the benefit of utilising in situ over bulk S/Se analyses in cases where more than one distinct paragenetically defined sulfide assemblage is present. Other disparities however, are less easily explained (e.g. RP04.23/392) and may indicate variability beyond the representativeness of the number of analyses we performed. Either way, it indicates the greater complexity of individual mineral S/Se systematics.

While the isotopic composition of coexisting pyrrhotite, pentlandite and chalcopyrite in the primary sulfides is rather consistent (Fig. 3), the S/Se ratios show greater variability both between and within the individual sulfide phases (Fig. 12A; Table 1). Furthermore, the secondary sulfides have S/Se ratios even more variable than the primary sulfides (Fig. 12B). The range in S/Se ratios is a true reflection on the variable Se contents of the pyrite, which is attributed to the extent to which the primary sulfide phases have been replaced and the ability of pyrite to inherit their Se contents. Thus it is unlikely these variations reflect simply the source of S and thus mineral-scale S/Se ratios have limited use as a reliable indicator of crustal S contribution. However, such variations must be controlled by other processes, and as such, S/Se ratios on this scale can be useful for tracing other ore forming processes.

Given the higher variability in S/Se ratio compared to the S isotopes, is it likely that S/Se ratios are more sensitive to other processes and therefore as a simple indicator of crustal contamination, we suggest S isotopes are more reliable. However, that is not to preclude the application of S/Se ratios to studies of crustal contamination, though it does require careful assessment of the rocks to identify any processes that may have been present that could alter an initial S/Se ratio *prior* to interpretation for S source. Contrary to this being problematic, it actually illustrates that S/Se ratios can be used to interpret a number of different syn- and post-magmatic processes *in addition* to crustal contamination.

With the well-defined primary sulfide assemblage and a low-temperature hydrothermal sulfide overprint, the GNPA member rocks provide an excellent opportunity to investigate two of these additional processes: (1) the partitioning behaviour of Se during magmatic sulfide fractionation processes and (2) during low temperature fluid alteration (<230 °C; Smith et al., 2011) which has not been previously attempted. Below, these are discussed prior to the process of crustal contamination, as interpretation of the latter requires a full appreciation of the effects of the former two.

10.3. Distribution and partitioning of Se in primary sulfide

Since there is greater analytical error associated with Se concentrations that are close to the detection limit of 60 ppm, in the following sections, values <80 ppm have been excluded when considering the partitioning behaviour of Se. The appreciable (80–164 ppm) and broadly comparable concentrations of Se in solid solution within coexisting primary pyrrhotite, pentlandite and chalcopyrite (average $Se_{(po)}/Se_{(pn)}$, $Se_{(po)}/Se_{(cpy)}$ and $Se_{(pn)}/Se_{(cpy)}$ ratios of 0.8 to 1.3; Table 3), indicates that Se partitions readily into each magmatic sulfide phase. Thus, Se is likely to be compatible within both high temperature monosulfide solid solution (mss) and intermediate solid solution (iss) and is not significantly partitioned by the lower temperature recrystallization of mss and iss to pyrrhotite-pentlandite-chalcopyrite.

The highest concentrations of Se are typically in either pyrrhotite or pentlandite, which contain near comparable Se contents (Table 3). From this, it can be suggested that Se is compatible in mss and during low temperature (<650 °C) recrystallization, it partitions equally into pyrrhotite or pentlandite. Pentlandite and pyrrhotite contain either comparable or slightly higher concentrations of Se to the coexisting Cu-sulfide. Thus, this may indicate evidence for slight preferential partitioning of Se into mss over iss. These features are not specific to the GNPA member or the Bushveld Complex, as LA-ICP-MS data available from the Jinchuan

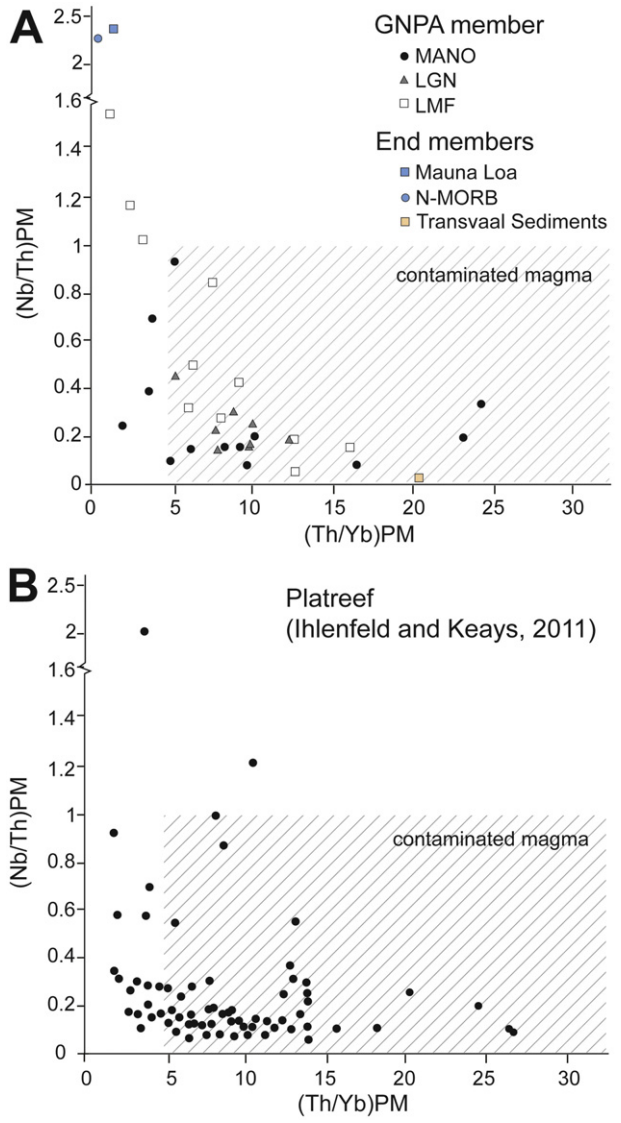

Fig. 10. A: Plot of $(Nb/Th)_{PM}$ vs $(Th/Yb)_{PM}$ for samples from the GNPA member. Average compositions of N-MORB, Hawaiian (Mauna Loa) tholeiites and Transvaal sediments are also shown for reference. B: comparison with $(Nb/Th)_{PM}$ and $(Th/Yb)_{PM}$ ratios from the Platreef (Ihlenfeld and Keays, 2011).

intrusion, China (Prichard et al., 2013), reveal comparable quantities of Se in solid solution within chalcopyrite (mean 133 ppm; n = 13), pyrrhotite (mean 151 ppm; n = 13) and pentlandite (mean 154 ppm; n = 13) with very similar average ratios of $Se_{(po)}/Se_{(pn)}$, $Se_{(po)}/Se_{(cpy)}$ and $Se_{(pn)}/Se_{(cpy)}$ of 0.98, 1.13, 1.15, respectively.

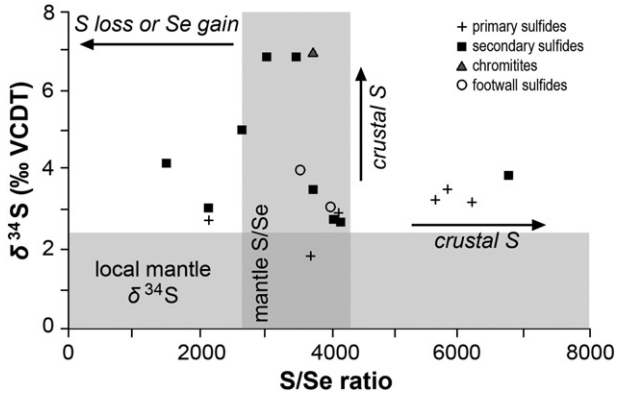

Fig. 11. Relationship between average $\delta^{34}S$ signature and bulk S/Se ratios in samples from Tables 1 and 2.

In contrast, experimental work by Helmy et al. (2010) constrained a $D_{Se}^{mss/sul}$ value of 0.6 ± 0.05, indicating Se preferentially fractionates into the residual Cu-rich sulfide liquid. This is consistent with differences observed in the Se concentration (and S/Se ratio) between the iss and mss fractions within a number of magmatic massive sulfide deposits such as Voisey's Bay, Sudbury and Noril'sk reported by Queffurus and Barnes (2015). The apparent disparities between the observations from these massive sulfides and the disseminated ores of Prichard et al. (2013) and this study may relate to different magmatic sulfide deposit types. Consequently, S/Se ratios provide insights into Se partitioning during sulfide liquid fractionation, and these effects must be considered prior to interpretation of them as a proxy for the source of S.

10.4. Mobility of Se during fluid alteration

Secondary pyrite and millerite were found to also host significant concentrations of Se in solid solution (Table 3) and $Se_{(py)}/Se_{(mil)}$ ratios vary slightly from 1.1 to 1.3 (Table 3). Concentrations of Se in pyrite appear broadly comparable or marginally elevated to the pyrrhotite it has replaced (Table 3), and it largely remains uniformly distributed throughout the primary relicts (Fig. 6E, F) at comparable concentrations to the completely unaltered samples (Fig. 6A-D). The Se concentrations in millerite are more variable, but are generally higher than the pentlandite it replaces (Table 3). As such, the secondary alteration appears to enrich the Se content of the secondary sulfides, consistent with the earlier discussion of there being a net S loss during the alteration process, which also increases the PGE tenor. This is consistent with the metasedimentary pyrite containing very low Se contents compared with pyrite formed from alteration of Se-rich magmatic pyrrhotite.

The presence of this secondary sulfide assemblage in the GNPA member provides an opportunity to explore the behaviour of Se during low temperature alteration. Similar low temperature assemblages have been recognised in a number of magmatic sulfide deposits (Dare et al., 2011; Djon and Barnes 2012; Piña et al. 2012). From our data it appears that Se is relatively immobile and remains within the sulfide, being taken up by both pyrite and millerite. Furthermore, the increase in Se tenor and reduction in S/Se ratio is consistent with there being bulk S loss during the alteration, indicating preferential S mobility. The lack of PGE mobilization (Smith et al., 2014) also shows that PGE are relatively immobile alongside Se under these conditions. While this attests to the immobility of PGE and Se during low temperature alteration of this kind, Prichard et al. (2013) have shown that Se can behave in a mobile manner, but only within saline, low pH, highly oxidizing fluids. The highly oxidising conditions required to remobilise Se in low temperature fluids (100–300 °C) are indicated in the Jinchuan intrusion by the unusual association of Se-bearing PGM with a magnetite–hematite alteration assemblage. The GNPA member and Platreef lack evidence of such assemblages and thus we infer that the fluid composition affecting the GNPA member were not suitable for remobilization of Se or PGE, but were responsible for the alteration of the sulfide assemblage.

Therefore, within most magmatic ore deposits, low temperature hydrothermal alteration that preferentially removes S over Se and PGE will act to increase the tenors of the sulfides in the secondary assemblages, with a concurrent *reduction* in S/Se. Therefore, it is essential to identify if any secondary hydrothermal activity has affected the S and Se contents before S/Se ratios are used to interpret the source of S. Furthermore, S/Se systematics can be used additionally to investigate S and Se mobility during low temperature alteration, alongside careful paragenetic studies.

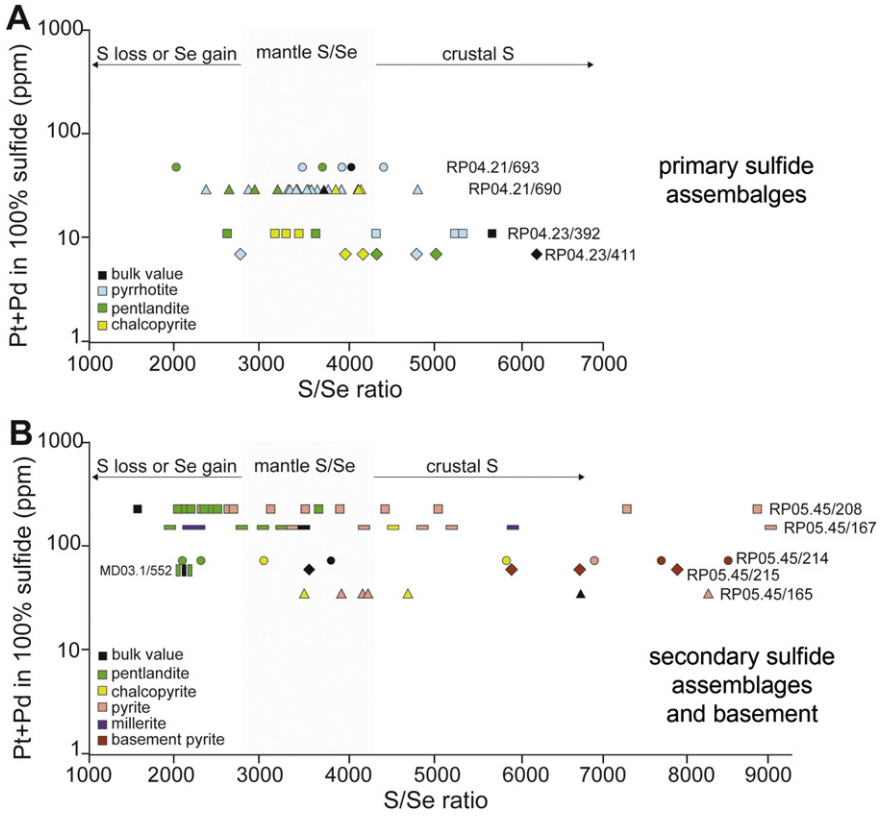

Fig. 12. Comparison of bulk S/Se ratios and the S/Se ratio of individual sulfide phases. All S/Se ratios are plotted against bulk Pt + Pd tenor for A: primary sulfide assemblages and B: secondary sulfide assemblages including footwall samples.

10.5. Crustal contamination and the source of S in the GNPA member

The above discussion demonstrates that where syn and/or post magmatic processes have significantly altered the initial composition of a sulfide liquid or sub-solidus assemblage, S/Se ratios need to be applied in conjunction with S isotopes and robust mineralogical understanding to confidently asses the role of contamination in ore genesis. Consequently, it is only through deciphering which indicator has been modified and by what process (es) that S isotopes and S/Se ratios are able to provide a truly reliable insight into the initial source of S. In addition, our trace element data allows us to assess crustal contamination that may be linked with the S addition, but also other contamination events, independently.

The dominance of δ^{34}S signatures in the GNPA member that are greater than the local mantle range (Fig. 3A, B) suggests that, similar to many other magmatic sulfide PGE-Ni–Cu deposits (e.g. Lesher and Groves 1986; Lesher and Burnham, 2001; Li et al., 2002; Ripley and Li, 2003), the addition of crustal S through assimilation of S-bearing country rocks was critical in the genesis of mineralization within the GNPA member. The relatively high S/Se ratios within some of the primary sulfides support this. Typically, contact-type PGE deposits are characterized by in situ contamination by local S-bearing country rocks, which can either be responsible for ore formation (e.g. Duluth Complex; Mainwaring and Naldrett, 1977; Ripley, 1981; Ripley et al., 1986 and the Basal Series of the Stillwater Complex; Lambert et al., 1994; Lee, 1996; McCallum, 1996) or simply overprint or modify an early developed crustal signature (e.g. Platreef; Holwell et al., 2007; McDonald and Holwell, 2007; Penniston-Dorland et al., 2008; Ihlenfeld and Keays, 2011). While Maier et al. (2008) inferred a local control over the δ^{34}S composition of sulfides within the GNPA member, the data in this study is inconsistent with the contribution of S from the local footwall as: (i) a crustal component is evident in sulfides developed east and west of the Grasvally Fault where underlain by quartzites and Lower Zone cumulates; and (ii) there is no evidence that the degree of contamination increases towards the footwall contact which is a feature commonly observed within the Platreef where the magma has sufficiently interacted with the local footwall (e.g. Sharman-Harris et al., 2005). In addition, the quartzites which underlie the GNPA member are themselves an unlikely source of S as although sufficiently high δ^{34}S values are found in pyrite (+3.5 up to +10‰; Table 1; Fig. 3), S-bearing minerals are relatively scarce throughout the Magaliesberg Quartzite Formation.

Although the use of S/Se ratios is complicated by the wider range of processes that can alter the ratio from its initial value as discussed above, preservation of crustal S/Se ratios within part of the primary sulfide assemblage in the GNPA provides evidence of an early contribution of crustal S, consistent with the S isotope signatures. As these high S/Se ratios (~6000) are preserved where the succession is underlain by Lower Zone cumulates, they also indicate that the GNPA magma was emplaced saturated in sulfide with a contaminated signature. Ihlenfeld and Keays (2011) used a similar argument for the Platreef, where areas underlain by S-poor granites and gneisses consistently showed crustal S/Se ratios.

As these findings are inconsistent with any model which involves the in situ development of a sulfide liquid, but yet are characterised by some crustal S, it is concluded that the magma from which the GNPA member crystallized was contaminated and saturated in S prior to emplacement. Our trace element data also shows evidence that the entire package was contaminated (Figs. 9, 10). The consistency of the primitive mantle-normalized spidergrams presented in Fig. 9 demonstrate that the GNPA magma (s) was characterised by pronounced negative Nb and Ti anomalies and LILE enrichment, features also reflected in the low $(Nb/Th)_{PM}$ ratios and high $(Th/Yb)_{PM}$ ratios (Fig. 10). Since these geochemical signatures are characteristic of crustal rocks and thus

considered indicative of crustal contamination of a mantle derived magma (Lightfoot and Hawkesworth, 1988; Lightfoot et al., 1990; Ihlenfeld and Keays, 2011), it is inferred that the parental magma(s) of the GNPA member were strongly crustally contaminated, almost exactly as shown by Ihlenfeld and Keays (2011) for the Platreef, prior to emplacement. Furthermore, this contaminant must have: (1) contained some crustal S, which was the trigger for sulfide saturation in the parental GNPA magma, consistent with the S isotope data; (2) been enriched in LILE; and (3) been characterised by elevated primitive mantle normalised Th/Yb ratios (> 15). Sharman et al. (2013) demonstrated that the crustal S present within the Platreef originated from shales or carbonates from the Duitschland Formation of the Transvaal Supergroup and on the basis of S isotope signatures, we suggest a similar source of crustal contaminant for the GNPA member. This is in agreement with a multi-stage emplacement model similar to that proposed for the Platreef (see Lee, 1996; Kinnaird, 2005; Holwell et al., 2007; McDonald and Holwell, 2007; Ihlenfeld and Keays, 2011; McDonald and Holwell, 2011) and for the rest of the Bushveld Complex (Penniston-Dorland et al., 2012).

An usual feature of the GNPA member is that the chromitites have very distinctive, anomalously heavy δ^{34}S compositions around 2‰ heavier than the rest of the magmatic succession. As this is such a lithology-specific feature it is possible that δ^{34}S was fractionated during the formation of the chromitites, though such fractionations are not documented and therefore speculative at best. Alternatively, they may represent a very particular, more contaminated magma event that triggered the formation of chromitites.

In contrast to this major pre-emplacement contamination event, the effects of later assimilation of crustal rocks are localised and preserved only where a metasedimentary footwall exists beneath the GNPA. Evidence of this second contamination event is only revealed by variations in the abundance of certain trace elements, and not in the S/Se ratios and S isotopes (as they only indicate contamination by S). Where the GNPA member is in contact with the Magaliesberg Quartzite Formation, a local footwall control over the REE signatures of the succession is clearly observed (Fig. 8). Here, the LMF especially, and the MANO unit to a lesser extent are characterised by: (i) elevated absolute concentrations of REE; (ii) enrichment in LILEs; and (iii) fractionation of LREE. As these features are more pronounced in the LMF unit that is in contact with the quartzites, it is concluded that a second contamination event resulted from the interaction of the GNPA magma with local footwall rocks at the time of emplacement, but that this did not input any crustal S. The Platreef also records a second, localised contamination event, but in many cases, this also includes the addition of S from a variety of other floor rocks (Sharman-Harris et al., 2005; Holwell et al., 2007).

Our work indicates that the S isotope signatures of the sulfides in the GNPA member are reliable indicators of the role of crustal S in ore genesis. However, it is important that in deposits where secondary sulfide overprints are identified, that the S isotope signatures of the most primary assemblages are sought for this purpose (Holwell et al., 2007). More generally, S isotope data can distinguish the sources of S in multi-stage sulfide parageneses; but only when coupled with robust mineralogy and petrology that clearly characterises different stages. Furthermore, trace element data can be utilized in concert to distinguish multiple stages of crustal contamination, with or without the addition of S.

10.6. A model for the emplacement of the GNPA member

In the northern limb of the Bushveld Complex, the Rustenburg Layered Suite has been disturbed by several phases of faulting, all of which are thought to post-date emplacement and consolidation of the intrusion (Truter, 1947; van Rooyen, 1954; de Villiers, 1967; van der Merwe, 1978; Hulbert, 1983). Although the relationship between the Platreef and GNPA member is masked by the NE trending Ysterberg-Planknek Fault, which marks the final episode of faulting within the southern sector of the limb, they are, considered by many to represent parts of the same succession (McDonald et al., 2005; Maier et al., 2008; van der Merwe, 2008; Grobler et al., 2012).

On the basis of several key observations that are presented in this, and previous work (Smith et al., 2011, 2014) it is envisaged that the GNPA member formed simultaneous to and in an analogous manner to the Platreef in multiple stages, and from one or a number of sub-chambers. Both deposits show similar constraints on the timing of emplacement, the timing of sulfide saturation and enrichment in PGE relative to the intrusion of Lower and Main Zone magmas, as indicated by field relations and the S isotope composition and S/Se ratio of the initial sulfide liquid. Furthermore, both show two distinct stages of contamination. From these relationships it can be inferred that both the Platreef and GNPA parental magmas were emplaced saturated in sulfide onto consolidated Lower Zone cumulates (van der Merwe, 1978; Kinnaird, 2005), contaminated in situ upon emplacement, and were significantly cooled prior to the intrusion of Main Zone magma, which throughout the northern limb was emplaced as a S-undersaturated, fertile magma with a separate PGE budget to the underlying PGE–Ni–Cu sulfide deposits (Holwell and Jordaan, 2006; Maier and Barnes, 2010; McDonald and Harmer, 2011; Lombard, 2012; Holwell et al., 2013).

A schematic summary of the proposed multi-stage model for the emplacement of the GNPA and Platreef, based on this, and a number of other studies cited here, is shown in Fig. 13 and can be summarised as follows:

- At depth in a staging chamber, magma passing through (possibly of Lower Zone composition) assimilates S-bearing and LILE enriched country rocks (Stage 1, Fig. 13A). Crustal S is likely derived from shales and carbonates of the Duitschland Formation and possibly other units of the Transvaal Supergroup. The contaminant is well homogenised with the magma, inducing sulfide saturation and development of an immiscible sulfide liquid (Stage 2, Fig. 13A).
- Sulfide droplets become enriched in PGE, Ni, Cu and semi-metals through interaction and processing of pre-GNPA magma (s) (Stage 3, Fig. 13A). It is possible that, like the Platreef, the GNPA member sourced its PGE content from the magma which was intruded to form the generally metal-depleted Lower zone intrusions, which cooled and solidified (McDonald and Holwell, 2007; McDonald et al., 2009; McDonald and Holwell, 2011; Stage 4, Fig. 13A).
- An early pulse of new magma invades previously established staging chambers, (Stages 5–7, Fig. 13B). This sulfide-bearing magma represents the parental magma to the GNPA member and possibly the Platreef. This magma then entrained and transported the pre-formed PGE-rich sulfides, and intruded into the Transvaal Supergroup to form the GNPA member and the Platreef (Stages 8-9, Fig. 13B).
- Multiple influxes of sulfide-bearing hybrid magma intruded into the Transvaal Supergroup to form the GNPA member.
- During emplacement, these magmas interacted with the local footwall rocks, with the GNPA assimilating some quartzite. In contrast to the Platreef at Turfspruit and Sandsloot, this second contamination event did not introduce additional crustal S into the system (Stage 10, Fig. 13B), with primary sulfides in the GNPA member retaining their initial crustal δ^{34}S signature. This event therefore had no control over ore genesis within the GNPA member, but did affect the sulfide content and PGM mineralogy of the Platreef (e.g. Hutchinson and Kinnaird, 2005; Holwell et al., 2007; Stage 10, Fig. 13B).
- Subsequent to emplacement, hydrothermal fluids, possibly derived from xenoliths of calc-silicates and other floor rocks, altered much of the primary sulfide and PGE mineralogy to a pyrite-millerite dominant assemblage (Smith et al., 2011). This low temperature alteration

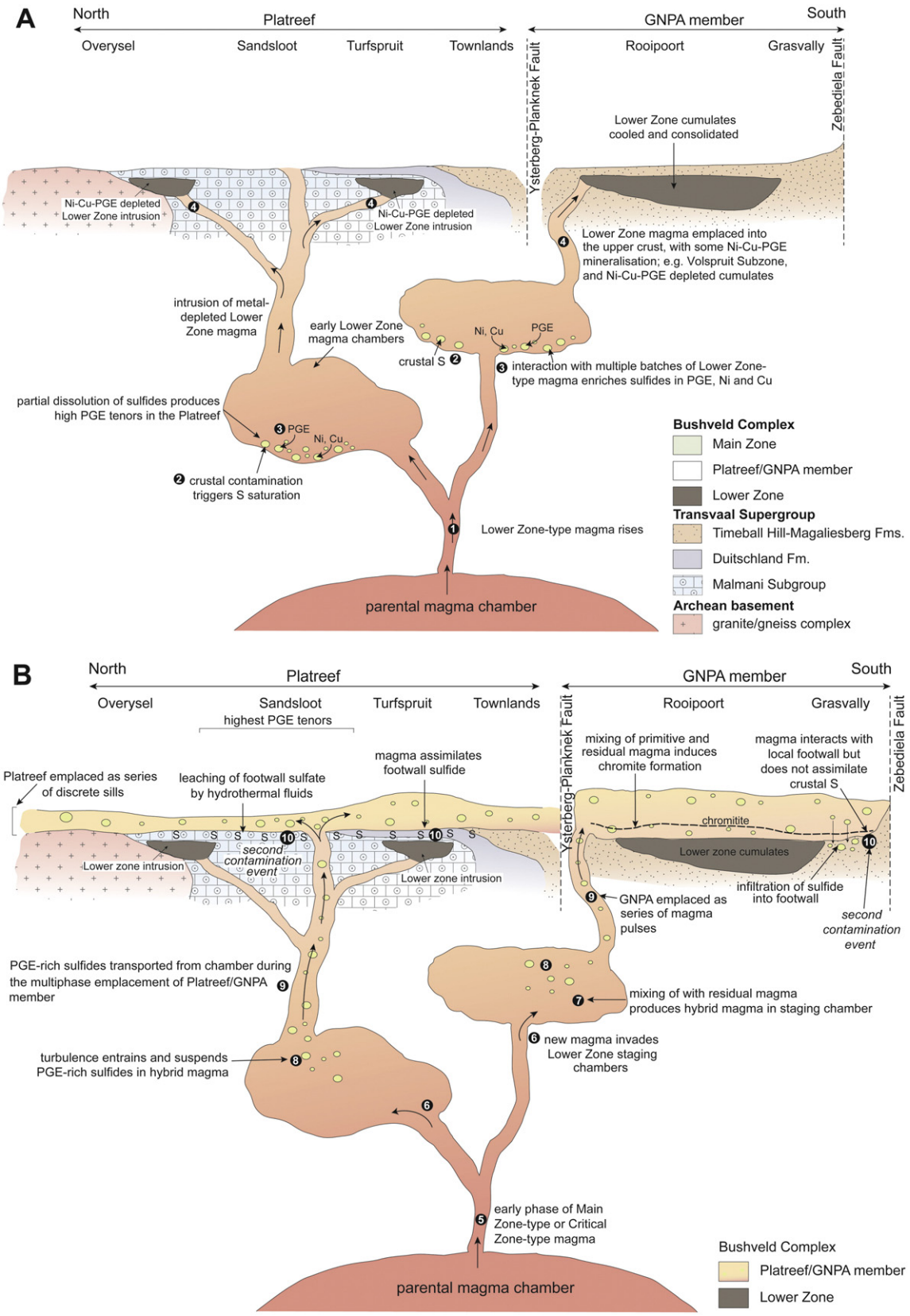

Fig. 13. A: Genetic model looking east, for the intrusion of Lower Zone-type, with sulfide immiscibility occurs in an intermediate staging chamber(s). See text for full explanation of numbered stages. B: Genetic model looking east, for the intrusion of Critical or Main zone type magma that mixes with residual magma to form hybrid magmas. These then entrained pre-formed sulfides to be emplaced as the GNPA member and the Platreef. See text for full explanation of numbered stages. C: Intrusion of the bulk of the Main Zone magma occurs after solidification of the GNPA member and Platreef. See text for full explanation of numbered stages.

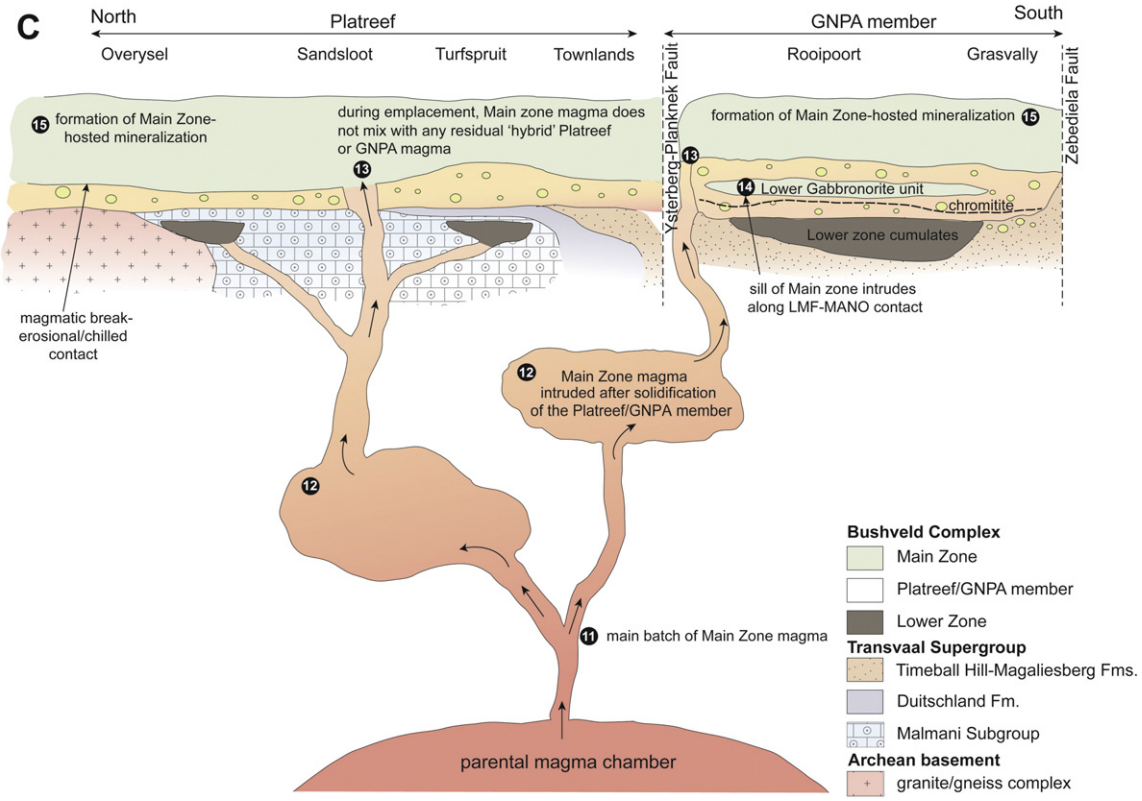

Fig. 13 (*continued*).

(<250 °C) resulted in: (i) S-loss, lowering the S/Se ratio to below the mantle range; (ii) $\delta^{34}S$ to fractionate by +1.5‰ during pyrite formation; (iii) the decoupling and remobilization of Pd, Au and to a lesser extent Cu from sulfides on a centimetre to decimetre scale (Smith et al., 2014); and (iv) the alteration of sulfide margins by tremolite, actinolite, chlorite and talc (Smith et al., 2011).

- Following the emplacement of the GNPA member and the Platreef a significant period of crystallization and cooling occurred (Holwell et al., 2005; Holwell and Jordaan, 2006).
- The rest of the Main Zone magma was then intruded as a PGE-fertile magma (Stages 11-13, Fig. 13C). This magma exploited the contact between the Lower Mafic and Mottled Anorthosite units to produce a sill of Main zone, represented by the Lower Gabbronorite unit (Stage 14, Fig. 12C) within the GNPA member.
- Sulfide saturation in the Main Zone magma formed the Ni–Cu–PGE mineralization (Stage 15, Fig. 13C) observed at Moorddrift (Maier and Barnes, 2010; Holwell et al., 2013), and other Main Zone hosted mineralization at the Aurora project (Maier et al., 2008) and the Waterberg area (Lombard, 2012).

11. Conclusions

Although the primary application of S isotopes and S/Se ratios is as independent tracers of the initial source of S in magmatic deposits, our case study illustrates that a number of syn- and post-magmatic processes may affect one, or both of these such that they may provide ambiguous data with respect to S source. Rather than these processes being problematic, variations in the $\delta^{34}S$ signature and in particular S/Se ratio can reveal a wealth of additional detail on a number of processes involved in the genetic history of a Ni–Cu–PGE deposit. However, a prerequisite for being able to do this is to utilize other independent petrological and mineralogical techniques that provide constraints on both the timing and effect of various ore-forming and modifying processes. Since the S/Se ratio is most susceptible to modification, this indicator has the ability to preserve detail on processes including: partial dissolution of sulfide, R-factor variations, hydrothermal alteration and S-loss. Utilizing both bulk and in situ methods in concert to determine the S/Se ratio allows for the assessment of multiple sulfide populations, the partitioning behaviour of Se during sulfide liquid fractionation and also the effects of low temperature fluid alteration. In comparison, S isotopes are relatively more robust and represent a more reliable indicator of the role of crustal S contamination, though the addition of trace element data can reveal multiple stages of contamination that do not necessarily include crustal S.

Acknowledgments

The authors would like to thank Caledonia Mining Corporation and in particular Trevor Pearton, for allowing access to the drillcore on the farms Rooipoort, Grasvally and Moorddrift; and Platinum Group Metals for allowing the sampling of core from War Springs. Review by Reid Keays is acknowledged for improving the clarity and structure of the manuscript, and editorial handling and review by Franco Pirajno. Jennifer Smith's Ph.D. research was funded by the Natural Environment Research Council (NE/1528426/1). The S isotope work was carried out via a NERC Facilities grant (IP/1280/1111) awarded to DAH at the Isotope Community Support Facility at SUERC. This work was part funded by a NERC SoS Minerals catalyst grant NE/L002191/1 awarded to the University of Leicester, and by a NERC SoS Consortium grant NE/M010848/1 "Te*a*Se: tellurium and selenium cycling and supply" awarded to the University of Leicester and Cardiff University. SUERC is supported by NERC and the Scottish Universities consortium.

Appendix A

Table A1
Bulk rock geochemistry for a suite of all units through the GNPA member.

		Borehole	RP04.23	RP04.23	RP04.23	RP04.23	RP04.23	RP04.23	RP05.45	RP05.45	RP05.45	RP05.45	RP05.45
		Sample	201	287	305	315	374	433	47	94	144	146	148
		Unit	MANO	LMF	LMF	LMF	LMF	LMF	LGN	LGN	LGN	LGN	LGN
wt.%	Method	Footwall	LZ	LZ	LZ	LZ	LZ	LZ	QTZ	QTZ	QTZ	QTZ	QTZ
SiO_2	XRF		56.59	53.11	50.17	61.43	50.27	52.19	52.12	52.5	53.04	52.96	53.23
TiO_2	XRF		0.06	0.45	0.1	0.11	0.15	0.12	0.39	0.52	0.56	0.36	0.41
Al_2O_3	XRF		30.66	13.59	16.78	29.11	14.61	6.14	18.17	17.53	17.2	15.63	17.69
Fe_2O_3	XRF		2.53	6.25	9.24	3.47	9.48	10.51	8.13	8.29	8.42	1.86	1.91
MnO	XRF		0.045	0.129	0.15	0.065	0.169	0.199	0.14	0.14	0.134	0.15	0.13
MgO	XRF		3.91	8.22	8.93	3.99	10.71	24.96	6.11	6.04	6.37	7.64	7.18
CaO	XRF		12.39	13.03	10.34	11.42	9.24	3.64	9.67	9.13	8.53	9.63	9.6
Na_2O	XRF		2.38	2.04	2.1	3.16	1.83	0.16	2.62	2.78	2.27	1.76	1.75
K_2O	XRF		0.537	0.886	0.366	0.793	0.645	0.564	0.731	1.036	1.161	0.44	0.48
P_2O_5	XRF		<0.001	0.055	<0.001	0.004	<0.001	0.008	0.051	0.09	0.092	0.08	0.07
SO_3	XRF		<0.002	0.003	0.26	0.003	0.009	<0.002	0.01	0.017	0.022		
CrO_3	XRF		0.045	0.116	0.187	0.114	0.145	0.208	0.056	0.054	0.073	0.03	0.1
NiO	XRF		0.042	0.036	0.247	0.01	0.044	0.13	0.016	0.011	0.014		
LOI			0.81	1.61	0.63	1.08	0.51	1.18	1.45	1.89	2.04	1.66	2.72
Total			110.01	99.53	99.5	114.76	97.8	100.01	99.65	100.04	99.92	92.2	95.28
ppm													
Rb	XRF		17.9	10.6	13.8	26.8	30.2	33.3	22.3	32.5	38.3	7.4	6.8
Sr	XRF		421.2	294.6	281.6	416.4	303.1	234.9	331.9	359.7	279.6	264	260.6
Y	XRF		1.3	6.9	3.2	2.9	5.2	3.7	13.9	15.9	19.4	11.1	13
Zr	XRF		3.2	32.3	3.4	6.4	3.9	15.3	46.6	53.2	45.7	49.2	61.7
Nb	XRF		1.7	1.3	2	0.6	0.3	0.9	2.7	3.7	4	1.98	4.61
Mo	XRF		0.9	1.3	1.7	0.9	1.4	1	1.7	1.5	1.5		
Pb	XRF		38.5	4.8	10.9	3.1	3.3	13.4	4.4	6	8		
Th	XRF		<0.5	1.1	0.7	0.7	<0.6	1.5	1.9	2.8	3.9	1.55	2.82
U	XRF		0.6	0.5	<0.5	<0.4	0.5	0.7	0.7	1.5	1	0.4	0.84
Ga	XRF		17.5	15.2	14.7	18.5	15.1	6.1	17.7	16.7	16.6	13.8	16.7
Zn	XRF		24	53.9	71.2	26.1	64.9	100.1	63.4	62.5	64	79.5	56.1
Cu	XRF		133.5	91.9	4576	57.9	242.3	28.5	47.8	44.7	59.4	168.7	59.8
Ni	XRF		347.7	212.1	1950.9	101.2	316.6	1064.8	142.9	108	135.7	530.8	195.4
Co	XRF		23.3	52	89.6	22.3	64.4	97.2	36.4	38.5	37.4	61.6	32.8
Cr	XRF		348.4	1276.2	1369.2	741.2	1048.4	1649.1	393.3	381	565.2	198.2	402.3
V	XRF		30.2	100.8	105.3	62.9	117.3	74.3	133.8	138.8	168.2	100.8	114.2
Sc	XRF		12.2	25.4	24	17.4	28.6	22.1	22.1	20.9	26.1	20.4	20
Ba	XRF		117	108.5	90.3	230.1	149.3	184.2	265	350.2	424.8	219.3	271.9
Cs	XRF		<1.9	<1.8	<1.8	<2.0	<1.7	<1.6	<1.7	<1.8	<1.7		
As	XRF		<0.5	<0.5	<0.6	<0.5	<0.5	<0.5	<0.5	2	4.2		
Sb	XRF		<1.0	<1.1	<1.1	<1.0	<1.1	<1.1	<1.1	<1.1	<1.1		
Se	XRF		<0.6	<0.6	3.4	<0.6	<0.7	<0.6	<0.6	<0.6	<0.6	0.4	
Sn	XRF		<0.8	<0.9	<1.0	<0.8	<1.0	<0.9	<0.9	<0.9	<1.0		
W	XRF		<1.0	<1.1	<1.4	<1.0	<1.2	<1.2	<1.2	<1.2	<1.2		
ppm													
La	ICP-MS		1.8	8.7	1.2	3.4	1.5	2.2	10.6	14.6	15.2	13.3	16.2
Ce	ICP-MS		3.5	22.6	2.6	6.7	3.5	4.4	22.7	30.4	31.5	24.6	29.7
Pr	ICP-MS		0.4	3.1	0.3	0.8	0.5	0.5	2.8	3.7	3.9	3	3.6
Nd	ICP-MS		1.3	12.8	1.3	2.7	2	1.7	10.4	13.8	14.5	11.2	13.5
Sm	ICP-MS		0.4	3.1	0.4	0.6	0.6	0.5	2.3	2.8	3	2.2	2.6
Eu	ICP-MS		0.4	0.9	0.4	0.6	0.5	0.2	0.8	0.9	1	0.8	0.9
Gd	ICP-MS		0.3	2.8	0.5	0.6	0.7	0.6	2	2.5	2.7	2.1	2.4
Tb	ICP-MS		0	0.5	0.1	0.1	0.1	0.1	0.4	0.4	0.4	0.3	0.4
Dy	ICP-MS		0.2	3.3	0.5	0.5	0.8	0.6	2.1	2.5	2.8	1.9	2.3
Ho	ICP-MS		0	0.6	0.1	0.1	0.1	0.1	0.4	0.5	0.5	0.4	0.5
Er	ICP-MS		0.1	1.9	0.3	0.3	0.5	0.4	1.2	1.4	1.6	1.1	1.3
Tm	ICP-MS		0	0.3	0.1	0	0.1	0.1	0.2	0.2	0.2	0.2	0.2
Yb	ICP-MS		0.1	2	0.4	0.3	0.6	0.5	1.2	1.5	1.6	1.1	1.3
Lu	ICP-MS		0	0.3	0.1	0	0.1	0.1	0.2	0.2	0.2	0.2	0.2
Hf	ICP-MS		0.3	8.1	0.4	0.5	0.5	0.6	1.9	1.8	1.3	1.2	1.6
Ta	ICP-MS		0.3	0.3	0.1	0.1	0.1	0.2	0.2	0.3	0.3	0.2	0.3
Pb	ICP-MS		33	30	7.8	3.3	2.9	10	4.4	6.8	5		
Th	ICP-MS		0.3	1.8	0.2	0.4	0.1	0.8	1.9	2.8	1.4	1.5	2.8
U	ICP-MS		0.1	0.7	0.1	0.1	0.1	0.3	0.5	0.6	0.3	0.4	0.8
Cr/MgO			89.1	155.3	153.3	185.8	97.9	66.1	64.4	63.1	88.7	25.9	56.0
Ce/Sm			8.8	7.3	6.5	11.2	5.8	8.8	9.9	10.9	10.5	11.2	11.4

Abbreviations:
MZ Main Zone
MANO Mottled Anorthosite unit
LGN Lower Gabbronorite unit
LMF Lower Mafic unit
LZ Lower zone
QTZ Quartzite

Table A1 continued

RP05.45	RP05.45	RP05.45	RP05.45	RP05.45	RP05.45	RP05.45	RP05.45	RP05.45	RP05.45	RP05.45	MD03.1	MD03.1
158	167a	167b	183	195	207	210	217a	217b	217c	219	552	582
LMF	LMF	LMF	LMF	LMF	LMF	LMF	FW	FW	FW	FW	MANO	MANO
QTZ	QTZ	QTZ	QTZ	QTZ	QTZ	QTZ	n/a	n/a	n/a	n/a	LZ	LZ
60.33	27.72	39.27	53.95	53.83	55.66	59.68					53.8	50.59
0.1	0.8	0.61	0.47	0.57	0.49	0.42					0.34	0.15
16.67	15.22	13.75	15.53	15.01	14.21	14.42					3.19	11.53
1.6	18.94	17.73	9.83	10.49	8.49	7.55					13.54	10.04
0.11	0.191	0.19	0.165	0.164	0.172	0.147					0.219	0.179
6.6	7.4	11.74	6.44	6.89	8.04	5.04					21.13	18.18
7.25	4.42	4.24	9.68	9.04	8.53	8.84					4.51	6.22
2.08	1.23	1.19	2.51	2.4	1.9	0.91					0.29	0.85
0.38	0.425	0.56	0.819	1.068	0.73	0.741					0.263	0.153
0.02	0.074	0.03	0.058	0.089	0.075	0.068					0.006	0.006
	0.118		<0.002	0.009	0.028	0.091					0.086	0.034
0.14	20.886	10.97	0.049	0.079	0.066	0.021					0.325	1.484
	0.438		0.012	0.015	0.016	0.013					0.771	0.162
1.02	0.57	0.92	0.58	0.53	1.53	2.17					1.34	0.41
96.31	98.43	101.21	100.09	100.18	99.94	100.12					99.8	99.98
ppm												
2.7	22.4	14.4015	24.7	30.2	22.1	29					17.1	7.6
414.7	189.8	182.7	332.3	289.5	256.1	211.2					23.2	156.5
10.1	13.4	11.2	15.4	21.2	17	17.5					12.8	3.6
30.8	77.2	74	69.1	54.9	49.4	86.7					46.3	12.9
1.28	4.7		3.2	4.4	3.9	4.6					2.8	0.7
	3.3		1.7	1.6	1.7	1.5					2.1	1.3
	19		4.8	7.4	14.1	10.4					11.1	5.8
2.59	2.8	3.02	2.6	3.2	3.6	5.2					2.9	0.8
0.72	0.4	1.03	0.6	1.4	1.4	1.8					1.7	<0.5
15.9	41.2	26.9109	16.9	16.8	13.5	15.8					6.4	9.8
33	328.6	353.8	67.5	78.6	105.7	59.2					93.1	79.1
39.4	8477.6	879.6	87.2	64.5	181.4	76.4					3758.9	657.6
149.2	4601.5	3010.2	117.2	135.7	149.5	121.7					5133.6	1117.1
30.1	207.7	142.5	49	49.2	46.7	34					121	89
984.9	108607	75151.8	404.1	572.8	493.1	174.4					2604.5	
70.7	1086.3	798.1	185.4	181.8	141.4	136.6					208.7	152.7
15.4	17.5	18.3	29.3	26	27.5	25.4					33.1	22.3
525.9	190.7	75.4	322.1	399.3	479.9	406.2					50.6	44.8
	<1.6		<1.8	<1.8	<1.7	<1.7					<1.6	<1.6
	1.7		<0.6	0.8	1.7	<0.5					7.2	2.4
	<1.5		<1.1	<1.1	<1.1	<1.0					<1.2	<1.1
	2		<0.7	<0.7	<0.6	<0.6					5	0.8
	<1.4		<1.0	<1.0	<0.9	0.9					<1.1	<1.0
	<2.4		<1.2	<1.3	<1.2	<1.1					<1.6	<1.3
ppm												
18.3	9.2	12.9	15.2	15.2	8.1	20.3	70.3	30.7	43.8	47.1	6	1.5
31.4	17.5	25	31.8	29.3	16.5	40.8	134.8	52.1	63.1	94.7	13.7	3.3
3.6	2	3	3.9	3.6	2.1	4.9	14.9	5.7	7.4	11.5	1.7	0.4
12.2	7.5	11.2	14.4	13.7	8.2	16.7	51.4	20	22.9	42	7	1.4
2.1	1.5	2.2	3	2.7	1.9	3.3	8.9	3.3	3.5	8	1.7	0.4
1.3	0.5	0.8	1.1	0.9	0.5	1	1.9	1.1	0.9	1.7	0.3	0.2
1.7	1.3	2	2.9	2.5	1.8	2.9	7.4	2.7	2.7	6.8	1.7	0.4
0.2	0.2	0.3	0.5	0.4	0.3	0.5	1.2	0.4	0.4	1	0.3	0.1
1.6	1.4	2	3	2.5	1.9	2.8	7.6	2.3	2.2	5.6	2.1	0.4
0.3	0.3	0.4	0.5	0.5	0.3	0.5	1.5	0.4	0.4	1	0.4	0.1
1	0.9	1.1	1.7	1.4	1	1.5	4.6	1.4	1.3	2.8	1.1	0.3
0.2	0.2	0.2	0.3	0.2	0.2	0.2	0.7	0.2	0.2	0.4	0.2	0.1
1.1	1	1.2	1.7	1.5	1.1	1.6	4.4	1.5	1.5	2.7	1.3	0.4
0.2	0.2	0.2	0.3	0.2	0.2	0.2	0.6	0.2	0.2	0.4	0.2	0.1
0.8	1.9	2	2.1	1.8	0.9	2.5	8.6	3	5.1	6	1.6	0.6
0.1	0.2	0.2	0.3	0.3	0.1	0.3	1.3	0.3	0.4	0.7	0.2	0.1
	57	10	6.3		10	9.3	33.7	26.4	20.5	17.3	9.2	4.6
2.6	3	2.3	2.5	3.2	1.8	4.7	27	1.4	12	2.9	2.4	0.3
0.7	1	0.7	0.7	0.9	0.5	1.7	5.7	0.6	3.3	1.1	0.7	0.1
149.2	14676.6	6401.3	62.7	83.1	61.3	34.6					123.3	
	11.7	11.4	10.6	10.9	8.7		15.1	15.8	18.0	11.8	8.1	8.3

(*continued on next page*)

Table A1 continued

	GV05.49	GV05.49	GV05.49	GV05.49	GV05.49	RP04.21	RP04.21	RP04.21	RP04.21	RP04.21	RP04.21	RP04.21	RP05.40
	30a	30b	40	45	45b	326	326	415a	415b	538	690a	690b	80
	MANO	MANO	LGN	LGN	LGN	MANO	MANO	MANO	MANO	MANO	MANO	MANO	MANO
wt.%	QTZ	QTZ	QTZ	QTZ	QTZ	QTZ	QTZ	QTZ	QTZ	QTZ	QTZ	QTZ	QTZ
SiO_2	52.27	54.34	53.74	54.14	54.16	52.66	52.69	50.91	51.79	50.72	45.95	40.57	51.4
TiO_2	0.41	0.45	0.41	0.34	0.51	0.13	0.24	0.08	0.15	0.17	0.17	0.07	0.12
Al_2O_3	18.06	19.53	17.24	19.49	16.7	18.83	16.02	20.36	22.49	23.17	18.48	22.8	19.93
Fe_2O_3	8.58	7.42	8.39	7.27	8.56	1.63	1.74	6.44	5.35	1.67	9.78	12.6	1.62
MnO	0.17	0.13	0.15	0.12	0.15	0.14	0.19	0.16	0.12	0.08	0.12	0.06	0.1
MgO	6.65	4.8	6.9	5.42	6.22	8.76	9.79	9.76	6.57	4.04	9.86	3.05	7.48
CaO	11.61	9.87	10.9	10.68	11.14	9.85	10.01	10.21	11.76	12.55	11.63	14.36	10.96
Na_2O	2.13	1.97	2.02	2.09	1.92	1.8	1.64	1.57	1.83	2.4	1.53	1.56	1.75
K_2O	0.47	0.56	0.39	0.55	0.41	0.15	0.18	0.14	0.32	0.47	0.23	0.8	0.17
P_2O_5	0.04	0.04	0.06	0.06	0.07	0.02	0.03	0	0.01	0.06	0.01	0.01	0.01
SO_3													
CrO_3	0	0	0	0	0	0.03	0.04			0.02			0.07
NiO											0.13	0.08	
LOI	0.44	1	0.3	0.48	0.32	0.29	0.27	0.39	0.58	0.8	1.26	2.82	1.09
Total	100.85	100.1	100.5	100.65	100.16	94.28	92.83	100	100.99	96.17	99.16	98.79	94.7
ppm													
Rb	10.33	11.467	7.7222	11.57	6.955	1.1	1.6	2.2417	7.4555	14.7	4.5552	19.864	1.7
Sr	304.8	349.8	301.9	339.3	294	237.4	203.8	244.7	295	330.4	294.6	269.3	338.2
Y	15.8	11.7	15.7	13.4	19.9	3	7.2	3.4	7.4	9.2	7.4	4.8	3.4
Zr	52.7	91.6	66.4	69.7	79.2	0.8	14.7	19.4	35.4	32.5	51.4	19.2	6.3
Nb						0.24	0.64			1.03			0.45
Mo													
Pb													
Th						0.12	0.75			1.39	0.78	0.03	0.37
U						0.03	0.21			0.36	0.27	0.07	0.1
Ga	16.55	17.302	16.094	17.072	16.548	15.2	13.5	13.98	16.5483	17.4			15.9
Zn	94.8	36.8	67.4	34.1	59.4	66	90.8	38	24.2	61	104.2	72	28.5
Cu	178	43	87.3	29.7	43.8	114.4	794.4	33.6	71.9	62.5	796.8	2584.8	33.1
Ni	129.9	113.1	145.6	89.3	125.7	254.8	1230.3	241.9	161.8	73.2	2973.5	4847.5	160.2
Co	39.8	28.1	36.8	30	38.5	41.8	59.7	33.5	24.9	26.9	115.9	232.6	29.7
Cr	414.7	266.3	325.3	327	360.7	228.9	240	524.5	339.6	165.5	896.6	518.4	478.7
V	101.7	95.5	109.3	97.2	140	94.7	128.5	88.2	92.9	100.3	86.7	96.5	66.5
Sc	29.3	18	28.5	20.6	33.7	17.8	23.7	16.5	17	16.1	20.7	13	13.4
Ba	54.7	97.1	68.2	71.1	64	75.9	94.6	13.9	30.2	159.3	34	82.8	118.5
Cs													
As													
Sb													
Se													
Sn													
W													
ppm													
La	9.7	13.6	12.3	13.1	14.7	2.9	5.7	1.9	5.3	8.4	4.3	2.8	3.7
Ce	19	25.2	23.9	24.9	29.8	4.5	10	3.1	9.8	16.3	8.6	4.9	6.2
Pr	2.4	2.9	2.9	3	3.8	0.5	1.3	0.3	1.2	2.1	1.1	0.6	0.8
Nd	9.5	10.2	11.3	11.1	14.7	1.9	4.9	1.3	4.6	7.5	4.2	2.2	2.9
Sm	2.2	2	2.5	2.2	3.2	0.4	1.1	0.3	1	1.6	1	0.5	0.6
Eu	0.7	0.7	0.8	0.9	0.9	0.5	0.5	0.3	0.5	0.7	0.4	0.4	0.5
Gd	2.1	1.7	2.3	2.1	3.1	0.4	1.2	0.2	1	1.5	0.9	0.5	0.6
Tb	0.4	0.3	0.4	0.3	0.5	0.1	0.2	0	0.2	0.2	0.2	0.1	0.1
Dy	2.2	1.7	2.3	1.9	3	0.5	1.3	0.3	1	1.4	1	0.5	0.6
Ho	0.4	0.3	0.4	0.4	0.6	0.1	0.3	0.1	0.2	0.3	0.2	0.1	0.1
Er	1.2	1	1.3	1.1	1.7	0.3	0.8	0.2	0.5	0.8	0.5	0.3	0.4
Tm	0.2	0.2	0.2	0.2	0.3	0.1	0.1	0	0.1	0.1	0.1	0	0.1
Yb	1.3	1	1.4	1.1	1.7	0.4	0.9	0.3	0.6	0.8	0.5	0.2	0.3
Lu	0.4	0.2	0.2	0.2	0.3	0	0.1	0	0.1	0.1	0.1	0	0
Hf	1.3	2.4	1.7	1.7	2	0.1	0.5	0.2	0.6	0.8	0.6	0.2	0.2
Ta	0.1	0.3	0.2	0.2	0.3	0	0.1	0	0.1	0.1	0.1	0	0
Pb	13	10	14	15	13			16	10.6		17	38	
Th	1.2	3.6	1.6	2.6	2.4	0.1	0.8	0.1	0.9	1.4	0.8	0	0.4
U	0.3	1	0.5	0.7	0.7	0	0.2	0	0.2	0.4	0.3	0.1	0.1
Cr/MgO	62.4	55.5	47.1	60.3	58.0	26.1	24.5	53.7	51.7	41.0	90.9	170.0	64.0
Ce/Sm	8.6	12.6	9.6	11.3	9.3	11.3	9.1	10.3	9.8	10.2	8.6	9.8	10.3

(*continued on next page*)

Table A1 continued

RP05.40	GV05.50	GV05.50	GV05.50	GV05.50	GV05.50	GV05.50	GV02.1	GV02.1	GV02.1	GV02.1	GV02.1	GV02.1
255	264	342	343	415	415	499	154	172	433	476	487	503
MANO	MANO	MANO	MANO	LGN	LGN	LGN	MANO	MANO	LMF	LMF	LMF	LMF
QTZ	QTZ	QTZ	QTZ	QTZ	QTZ	QTZ						
53.8	51.3	53.84	54.43	53.65	53.85	52.9						
0.36	0.23	0.11	0.14	0.45	0.47	0.43						
18.1	19.67	23.47	18.63	17.08	18.11	16.78						
1.86	1.73	1.61	1.64	1.95	1.97	1.93						
0.12	0.11	0.05	0.11	0.13	0.13	0.13						
6.18	7.58	2.38	5.65	6.9	6.75	6.79						
10.02	10.6	10.35	10.41	9.79	9.91	9.74						
2.17	2.22	3.07	2.3	2.16	2.17	2.44						
0.38	0.3	1.13	0.52	0.46	0.43	0.69						
0.08	0.02	0.01	0.01	0.08	0.08	0.08						
0.05	0.1	0.02	0.05	0.07	0.07	0.06						
1.25	1.09	2.1	0.44	0.24	0.35	1.28						
94.37	94.96	98.14	94.33	92.97	94.29	93.26						
ppm												
4.3	9.7	65.6	16.6	6.2	4.1	21.7						
321	318.1	389.8	311.9	286.8	306.8	321.9						
12.2	5.9	4.2	6.1	12.5	13.2	14.6						
39.3	23.9	20.6	20.3	77.7	30.7	54.5						
2.25	1.4	0.92	0.82	3.29	2.97	4.23						
1.69	1.05	1.23	1.44	2.25	2.16	2						
0.48	0.31	0.38	0.37	0.62	0.6	0.5						
16.9	16.4	16.7	15	16.3	17	15.1						
47.3	74.3	52.5	63.1	56.3	58.1	97.4						
65.7	55.2	214.6	100.9	57.4	33.6	99.2						
135	253.6	6.6	75	122.3	130	133.4						
32.7	39.6	14.2	33.8	36	35.5	45.3						
363	652.5	160	342.8	513.1	510	436.9						
112.7	108.6	86.3	97.9	129.5	128.2	139.1						
20.3	18.4	10.1	18.5	21.1	20.3	23.8						
228.2	133	324.5	233.9	218.5	261.3	231.9						
ppm												
12	6.2	8.1	7.3	14.4	16.1	14.6	3.8	7.9	2.2	6.9	4	4
22.5	11.6	14	13.3	26.5	30	28.6	8.4	15.6	4.1	15.3	8	8.9
2.8	1.5	1.6	1.6	3.3	3.7	3.7	1.1	1.7	0.5	1.9	0.9	1.1
10.7	5.4	5.2	5.7	12.3	13.4	13.4	4.6	6	2.1	7.6	3.4	4.8
2.1	1.1	1.1	1.2	2.4	2.7	2.8	1.2	1.2	0.6	1.8	0.8	1.2
0.9	0.6	0.6	0.6	0.9	0.9	0.9	0.5	0.8	0.4	0.6	0.4	0.5
2	1.1	0.8	1.1	2.4	2.5	2.7	1.3	1	0.6	1.7	0.9	1.2
0.3	0.2	0.1	0.2	0.4	0.4	0.4	0.2	0.1	0.1	0.3	0.2	0.2
2	1	0.7	1	2.2	2.2	2.6	1.8	0.8	0.7	1.8	1	1.4
0.4	0.2	0.1	0.2	0.4	0.5	0.5	0.3	0.1	0.1	0.3	0.2	0.3
1.1	0.6	0.4	0.6	1.3	1.3	1.4	1.1	0.4	0.4	1	0.6	0.8
0.2	0.1	0.1	0.1	0.2	0.2	0.2	0.2	0.1	0.1	0.1	0.1	0.1
1.2	0.6	0.4	0.6	1.3	1.2	1.5	1.4	0.4	0.5	1	0.8	0.9
0.2	0.1	0.1	0.1	0.2	0.2	0.2	0.2	0.1	0.1	0.1	0.1	0.1
1	0.7	0.6	0.6	1.8	0.9	1.5	0.6	0.7	0.6	1.4	1	0.8
0.2	0.1	0.1	0.1	0.2	0.2	0.2	0.1	0.2	0.1	0.1	0.2	0.1
							4.7	13	1.2	8.4	11	12
1.7	1	1.2	1.4	2.2	2.2	2	0.9	1.8	0.2	2.3	0.9	1
0.5	0.3	0.4	0.4	0.6	0.6	0.5	0.2	0.5	0.1	0.7	0.2	0.2
58.7	86.1	67.2	60.7	74.4	75.6	64.3						
10.7	10.5	12.7	11.1	11.0	11.1	10.2	7.0	13.0	6.8	8.5	10.0	7.4

References

Barnes, S.-J., Lightfoot, P.C., 2005. Formation of magmatic nickel-sulfide ore deposits and processes affecting their copper and platinum-group element contents. In: Hedenquist, J.W., Thompson, J.F.H., Goldfarb, R.J., Richards, J.P. (Eds.), Economic Geology 100th Anniversary Volume, pp. 179–213.

Barnes, S.-J., Savard, D., Bédard, P., Maier, W.D., 2009. Selenium and sulfur concentrations in the Bushveld Complex of South Africa and implications for formation of the platinum-group element deposits. Mineral. Deposita 44, 647–663.

Brenan, J.M., 2015. Se-Te fractionation by sulfide–silicate melt partitioning: implications for the composition of mantle-derived magmas and their melting residues. Earth Planet. Sci. Lett. 422, 45–57.

Buchanan, D.L., Nolan, J., Suddaby, P., Rouse, J.E., Viljoen, M.J., Davenport, J.W.J., 1981. The genesis of sulfide mineralization in a portion of the Potgietersrus limb of the Bushveld Complex. Econ. Geol. 76, 568–579.

Cameron, E.M., 1982. Sulphate and sulphate reduction in early Precambrian oceans. Nature 296, 145–148.

Cawthorn, R.G., Meyer, F.M., 1993. Petrochemistry of the Okiep copper district basic intrusive bodies, northwestern Cape province, South Africa. Econ. Geol. 88, 590–605.

Chambers, L.A., Trudinger, P.A., 1979. Microbiological fractionation of stable sulfur isotopes: a review and critique. J. Geomicrobiol. 1, 249–293.

Dare, S.A.S., Barnes, S.-J., Prichard, H.M., Fisher, P.C., 2011. Chalcophile and platinum-group element (PGE) concentrations in the sulfide minerals from the McCreedy East deposit, Sudbury, Canada, and the origin of PGE in pyrite. Mineral. Deposita 46, 381–407.

Dare, S.A.S., Barnes, S.-J., Prichard, H.M., Fisher, P.C., 2014. Mineralogy and geochemistry of Cu-rich ores from the McCreedy East Ni–Cu–PGE deposit (Sudbury, Canada): implications for the behaviour of platinum group and chalcophile elements at the end of crystallization of a sulfide liquid. Econ. Geol. 109, 343–366.

de Klerk, L., 2005. Bushvled STRATIGRAPHY on Rooipoort, Potgietersrus Limb [abs.]. Platreef Workshop, 2nd, Mokopane, South Africa, 28th–30th October 2005, Abstracts.

Djon, M.L.N., Barnes, S.-J., 2012. Changes in sulphides and platinum-group minerals with the degree of alteration in the Roby, Twilight, and High Grade Zones of the Lac des Iles Complex, Ontario. Canada. Mineral. Deposita 47, 875–896.

Dreibus, G., Palme, H., Spettek, B., Zipfel, J., Wanke, H., 1995. Sulfur and selenium in chondritic meteorites. Meteoritics 30, 439–445.

Eales, H.V., Cawthorn, R.G., 1996. The bushveld complex. In: Cawthorn, R.G. (Ed.) Layered Intrusions. Elsevier Science 181–230.

Eckstrand, O.R., Cogolu, E., 1986. Se/S evidence relating to genesis of sulphides in the Crystal Lake gabbro, Thunder Bay, Ontario. Geological Association of Canada – Abstract Programs. 11, p. 66.

Eckstrand, O.R., Hulbert, L.J., 1987. Selenium and the source of sulfur in magmatic nickel and platinum deposits (abs): Geological Association of Canada–Mineralogical Association Canada Program with Abstracts. v.12 p. 40.

Eckstrand, O.R., Grinenko, L.N., Krouse, H.R., Paktunc, A.D., Schwann, P.L., Scoates, R.F., 1989. Preliminary data on sulphur isotopes and Se/S ratios, and the source of sulphur in magmatic sulphides from the Foz River Sill, Molson Dykes and Thompson nickel deposits, northern Manitoba. Current Research, Part C. Geological Survey of Canada Paper 235–242.

Ewers, G.R., 1977. Experimental hot water-rock interactions and their significance to natural hydrothermal systems in New Zealand. Geochim. Cosmochim. Acta 41, 143–150.

Grassineau, N.V., Appel, P.W.U., Fowler, C.M.R., Nisbet, E.G., 2005. Distinguishing biological from hydrothermal signatures via sulphur and carbon isotopes in Archaean mineralisations at 3.8 and 2.7 Ga. In: McDonald, I., Boyce, A.J., Butler, I.B., Herrington, R.J., Polya, D.A. (Eds.), Mineral Deposits and Earth Evolution. Geol Soc London 248, pp. 195–212 (special publication).

Grinenko, L.I., 1985. Sources of sulfur of the nickeliferous and barren gabbro-dolerite intrusions of the northwest Siberian platform. Int. Geol. Rev. 27, 695–708.

Grobler, D.F., Nielsen, S.A., Broughton, D.W., 2012. Upper Critical Zone (Merenksy Reef) correlates within the Platreef on Turfspruit 241KR, northern limb, Bushveld Complex. Platreef Workshop, 5th, Mokopane, South Africa, 9th–11th November 2012, Abstracts.

Habicht, K., Canfield, D.E., 1997. Sulfur isotope fractionation duringbacterial sulfate reduction in organic-rich sediments. Geochim. Cosmochim. Acta 61, 5351–5361.

Hattori, K.H., Arai, S., Clarke, D.B., 2002. Selenium, tellurium, arsenic and antimony contents of primary mantle sulfides. Can. Mineral. 40, 637–650.

Helmy, H.M., Ballhaus, C., Wohlgemuth-Ueberwasser, C., Fonseca, R.O., Laurenz, V., 2010. Partitioning of Se, As, Sb, Te and Bi between monosulfide solid solution and sulfide melt—application to magmatic sulfide deposits. Geochim. Cosmochim. Acta 74, 6174–6179.

Hinchey, J.G., Hattori, K.H., 2005. Magmatic mineralization and hydrothermal enrichment of the high grade zone at the Lac des Iles palladium mine, northern Ontario, Canada. Mineral. Deposita 40, 13–23.

Holwell, D.A., Jordaan, A., 2006. Three-dimensional mapping of the Platreef at the Zwartfontein South mine: implications for the timing of magmatic events in the northern limb of the Bushveld Complex, South Africa. Appl. Earth Sci. 115, B41–B48.

Holwell DA, Armitage PEB, McDonald I (2005) Observations on the relationship between the Platreef and its hangingwall. Appl. Earth Sci., v. 114, p. B225–B241.

Holwell, D.A., Boyce, A.J., McDonald, I., 2007. Sulfur isotope variations within the Platreef Ni–Cu–PGE deposit: genetic implications for the origin of sulfide mineralization. Econ. Geol. 102, 1091–1110.

Holwell, D.A., McDonald, I., Butler, I.B., 2011. Precious metal enrichment in the Platreef, Bushveld Complex, South Africa: evidence from homogenized magmatic sulfide melt inclusions. Contrib. Mineral. Petrol. 161, 1011–1026.

Holwell, D.A., Jones, A., Smith, J.W., Boyce, A.J., 2013. New mineralogical and isotopic constraints on main zone-hosted PGE mineralisation at Moorddrift, northern Bushveld Complex. Mineral. Deposita 48, 675–686.

Holwell, D.A., Keays, R.R., Firth, E.A., Findlay, J., 2014. Geochemistry and Mineralogy of Platinum-group Element Mineralization in the River Valley Intrusion, Ontario, Canada: A Model for Early Stage S Saturation and Multi-stage Emplacement and the Implications for 'Contact-type' Ni–Cu–PGE Mineralization. Econ. Geol.

Holwell, D.A., Keays, R.R., McDonald, I., Williams, M.R., 2015. Extreme enrichment of PGE, Au, Se and Te by sulfide droplets in closed system magma chambers: evidence from LA-ICP-MS analysis of sulfide microdroplets in the Skaergaard Intrusion, east Greenland. Contrib. Miner. Petrol. http://dx.doi.org/10.1007/s00410-015-1203-y (in press).

Howard, J.H., 1977. Geochemistry of selenium: formation of ferroselite and selenium behavior in the vicinity of oxidizing sulfide and uranium deposits. Geochim. Cosmochim. Acta 41, 1665–1678.

Hulbert LJ (1983) A Petrographical Investigation of the Rustenburg Layered Suite and Associated Mineralization South of Potgietersrus. Unpublished D.Sc. Dissertation, Pretoria, South Africa, The University of Pretoria.

Hutchinson D, Kinnaird JA (2005) Complex multistage genesis for the Ni–Cu–PGE mineralization in the southern region of the Platreef, Bushveld Complex, South Africa. Appl. Earth Sci., v. 114, p. B208–B223.

Ihlenfeld, C., Keays, R., 2011. Crustal contamination and PGE mineralization in the Platreef, Bushveld Complex, South Africa: evidence for multiple contamination events and transport of magmatic sulfides. Mineral. Deposita 46, 813–832.

Kelley, S.P., Fallick, A.E., 1990. High precision spatially resolved analysis of $\delta^{34}S$ in sulfides using a laser extraction system. Geochim. Cosmochim. Acta 54, 883–888.

Kerr, A., Leitch, A.M., 2005. Self destructive sulfide segregation systems and the formation of high-grade magmatic ore deposits. Econ. Geol. 100, 311–332.

Kinnaird, J.A., 2005. Geochemical evidence for multiphase emplacement in the southern Platreef. Appl. Earth Sci. 114, B225–B241.

Lambert, D.D., Walker, R.J., Morgan, J.W., Shirey, S.B., Carlson, R.W., Zientek, M.L., Lipin, B.R., Koski, M.S., Cooper, R.L., 1994. Re—Os and Sm—Nd isotope geochemistry of the Stillwater Complex, Montana: implications for the petrogenesis of the J–M reef. J. Petrol. 35, 1717–1753.

Lee, C.A., 1996. A review of mineralization in the Bushveld Complex and some other layered mafic intrusions. In: Cawthorn, R.G. (Ed.), Layered intrusions. Elsevier Science, pp. 103–146.

Lesher, C.M., 1986. Groves DG (1986) Controls on the formation of komatiite-associated nickel–copper sulphide deposits. In: Friedrich, G.H., et al. (Eds.), Geology and Metallogeny of Copper Deposits. Proc. 25th Int. Geol. Congr. Moscow, Springer, Berlin, pp. 43–62

Lesher, C.M., Burnham, O.M., 2001. Multicomponent elemental and isotopic mixing in Ni–Cu–(PGE) ores at Kambalda, Western Australia. Can. Mineral. 39, 421–446.

Lesher, C.M., Groves, D.G., 1986. Controls on the formation of komatiite-associated nickel-copper sulphide deposits. In: Friedrich, G.H., et al. (Eds.), Geology and Metallogeny of Copper Deposits. Springer, Berlin, pp. 43–62.

Lesher, C.M., Keays, R.R., 2002. Komatiite-associated Ni–Cu–(PGE) deposits: geology, mineralogy, geochemistry and genesis. Can. Instit. Min. Metall. Pet. Special Volume 54, 579–618.

Li, C., Ripley, E.M., Maier, W.D., Gomwe, T.E.S., 2002. Olivine and sisotopic compositions of the Uitkomst Ni–Cu sulfide ore-bearing complex, South Africa: evidence for S contamination and multiple magma emplacements. Chem. Geol. 188, 149–159.

Lightfoot, P.C., Hawkesworth, C.J., 1988. Origin of Deccan Trap lavas: evidence from combined trace element and Sr–Nd-and Pb-isotope studies. Earth Planet. Sci. Lett. 91, 89–104.

Lightfoot, P.C., Keays, R.R., 2005. Siderophile and chalcophile metal variations in flood basalts from the Siberian trap, Noril'sk region: implications for the origin of the Ni–Cu–PGE sulfide ores. Econ. Geol. 100, 439–462.

Lightfoot, P.C., Hawkesworth, C.J., Devey, C.W., Rogers, N.W., Van Calsteren, P.W.C., 1990. Source and differentiation of Deccan Trap lavas: implications of geochemical and mineral chemical variations. J. Petrol. 31, 1165–1200.

Lombard, K., 2012. Exploration Results and Mineral Resource Estimate for the Waterberg Platinum Project: Coffey Mining, South Africa (89 pp.).

Lorand, J.P., Alard, O., Luguet, A., Keays, R.R., 2003. Sulfur and selenium systematics of the subcontinental lithospheric mantle: inferences from the Massif Central xenolith suite (France). Geochim. Cosmochim. Acta 67, 4137–4151.

Lorand, J.P., Luguet, A., Alard, O., 2013. Platinum-group element systematics and petrogenetic processing of the continental upper mantle: A review. Lithos 167, 2–21.

Maier, W.D., Barnes, S.-J., 1996. Unusually high concentrations of magnetite at Caraiba and other Cu-sulfide deposits in the Curaca Valley, Bahia, Brazil. Can. Mineral. 34, 717–731.

Maier, W.D., Barnes, S.-J., 1998. Concentrations of rare earth elements in silicate rocks of the lower, critical and main zones of the Bushveld Complex. Chem. Geol. 150, 85–103.

Maier, W.D., Barnes, S.-J., 2010. The petrogenesis of platinum-group element reefs in the upper main zone of the northern lobe of the Bushveld Complex on the farm Moorddrift. S. Afr./Econ. Geol. 105, 841–854.

Maier, W.D., de Klerk, W.J., Teigler, B., Mitchell, A.A., 1996. Cu/Pd and Cu/Pt of silicate rocks in the Bushveld Complex: implications for platinum-group element exploration. Econ. Geol 91, 1151–1158.

Maier, W.D., de Klerk, L., Blaine, J., Manyeruke, T., Barnes, S.-J., Stevens, M.V.A., Mavrogenes, J.A., 2008. Petrogenesis of contact-style PGE mineralization in the northern lobe in the Bushveld Complex: comparison of data from the farms Rooipoort, Townlands, Drenthe and Nonnenweth. Mineral. Deposita 43, 255–280.

Mainwaring, P.R., Naldrett, A.J., 1977. Country-rock assimilation and the genesis of Cu–No sulfides in the Waterhen intrusion, Duluth Complex, Minnesota. Econ. Geol. 72, 1269–1284.

Manyeruke, T.D., Maier, W.D., Barnes, S.-J., 2005. Major and trace element geochemistry of the Platreef on the farm townlands, northern Bushveld Complex. S. Afr. J. Geol. 108, 381–396.
McCallum, I.S., 1996. The stillwater complex. In: Cawthorn, R.G. (Ed.), Layered Intrusions. Elsevier Science, pp. 441–484.
McDonald, I., Harmer, R.E., 2011. Cu–Ni–PGE mineralisation at Aurora is not Platreef, so where does it fit in? Platreef Workshop, 4th, Mokopane, South Africa, 14th–16th January 2011, Abstracts
McDonald, I., Holwell, D.A., 2007. Did lower zone magma conduits store PGE-rich sulphides that were later supplied to the Platreef? S. Afr. J. Geol. 110, 611–616.
McDonald, I., Holwell, D.A., 2011. Geology of the northern Bushveld Complex and the setting and genesis of the Platreef Ni–Cu–PGE deposit. Rev. Econ. Geol. 17, 297–327.
McDonald, I., Viljoen, M.J., 2006. Platinum-group element geochemistry of mantle eclogites: a reconnaissance study of xenoliths from Orapa kimberlite. Botswana. Appl. Earth Sci. (Trans. Inst. Min. Metall. B) 115, 81–93.
McDonald, I., Holwell, D.A., Armitage, P.E.B., 2005. Geochemistry and mineralogy of the Platreef and 'critical zone' of the northern lobe of the Bushveld Complex, South Africa: implications for Bushveld stratigraphy and the development of PGE mineralization. Mineral. Deposita 40, 526–549.
McDonald I, Holwell DA, Wesley B (2009) Assessing the potential involvement of an early magma staging chamber in the generation of the Platreef Ni–Cu–PGE deposit in the northern limb of the Bushveld Complex: a pilot study of the Lower Zone Complex at Zwartfontein. Appl. Earth Sci., v. 118, p.B5–B20.
McDonald, I., Jones, R.E., Holwell, D.A., Butler, I.B., 2012. Platinum-group element tenors and S/Se ratios of Platreef sulphide melt inclusions [abs.]. Platreef Workshop, 5th, Mokopane, South Africa, 9th–12th January 2012, Abstracts.
McDonough, W.F., Sun, S.S., 1995. The composition of the earth. Chem. Geol. 120, 223–253.
Miyoshi, T., Sakai, H., Chiba, H., 1984. Experimental study of sulfur isotope fractionation factors between sulfate and sulfide in high temperature melts. Geochem. J. 18, 75–84.
Mungall, J.E., Brenan, J., 2014. Partitioning of platinum-group elements and Au between sulfide liquid and basalt and the origins of mantle–crust fractionation of the chalcophile elements. Geochim. Cosmochim. Acta 125, 265–289.
Naldrett, A.J., 2011. Fundamentals of magmatic sulfide deposits. Rev. Econ. Geol. 17, 1–50.
Naldrett, A.J., Wilson, A., Kinnaird, J.A., Chunnett, G., 2009. PGE tenor and metal ratios within and below the Merensky Reef, Bushveld Complex: implications for its genesis. J. Petrol. 50, 625–659.
Ohmoto, H., Rye, R.O., 1979. Isotopes of sulfur and carbon. In: Barnes, H.L. (Ed.), Geochemistry of Hydrothermal Ore Deposits, 2nd ed. John Wiley and Sons, London, pp. 509–567.
Patten, C., Barnes, S.J., Mathez, E.A., Jenner, F.E., 2013. Partition coefficients of chalcophile elements between sulfide and silicate melts and the early crystallization history of sulfide liquid: LA-ICP-MS analysis of MORB sulfide droplets. Chem. Geol. 358, 176–188.
Peach, C.L., Mathez, E.A., Keays, R.R., 1990. Sulfide melt-silicate melt distribution coefficients for the noble metals and other chalcophile metals as deduced from MORB: implications for partial melting. Geochem. Cosmochim. Acta 54, 3379–3389.
Peck, D.C., Keays, R.R., 1990. Insights into the behaviour of precious metals in primitive, S-undersaturated magmas; evidence from the Heazlewood River Complex, Tasmania. Can. Mineral. 28, 553–577.
Penniston-Dorland, S.C., Wing, B.A., Nex, P.A.M., Kinnaird, J.A., Farquhar, J., Brown, M., Sharman, E.R., 2008. Multiple sulfur isotopes reveal a magmatic origin for the Platreef platinum group element deposit, Bushveld Complex, South Africa. Geology 36, 979–982.
Penniston-Dorland, S.C., Mathez, E.A., Wing, B.A., Farquhar, J., Kinnaird, J.A., 2012. Multiple sulfur isotope evidence for surface-derived sulfur in the Bushveld Complex. Earth Planet Sci. Lett. 337-338, 236–242.
Piña, R., Gervilla, F., Barnes, S.-J., Ortega, L., Lunar, R., 2012. Distribution of platinum-group and chalcophile elements in the Aguablanca Ni-Cu sulfide deposit (SW Spain): Evidence from a LA-ICP-MS study. Chem. Geol. 302–303, 61–75.
Prichard, H.M., Knight, R.D., Fisher, P.C., McDonald, I., Zhou, M.-F., Wang, C.Y., 2013. Distribution of platinum-group elements in magmatic and altered ores in the Jinchuan intrusion, China: an example of selenium remobilization by post magmatic fluids. Mineral. Deposita 48, 767–786.
Queffurus M, Barnes S-J (2015) A review of sulfur to selenium ratios in magmatic nickel–copper and platinum-group element deposits. Ore Geol. Rev., v. 69, p. 301-324.
Ripley, E.M., 1981. Sulfur isotopic abundances of the Dunka Road Cu–Ni deposit, Duluth Complex, Minnesota. Econ. Geol. 76, 619–620.
Ripley, E.M., 1990. Se/S ratios of the Virginia Formation and Cu–Ni mineralization in the Babbitt area, Duluth Complex, Minnesota. Econ. Geol. 85, 1935–1940.
Ripley, E.M., Li, C., 2003. Sulfur isotope exchange and metal enrichment in the formation of magmatic Cu–Ni–(PGE) deposits. Econ. Geol. 98, 635–641.
Ripley, E.M., Lambert, D.D., Frick, L.R., 1986. Re–Os, Sm–Nd, and Pd isotopic constraints on mantle and crustal contributions to magmatic sulfide mineralization in the Duluth Complex. Geochim. Cosmochim. Acta 62, 3349–3365.
Ripley, E.M., Li, C., Shin, D., 2002. Paragenesis assimilation in the genesis of magmatic Ni–Cu–Co sulfide mineralization at Voisey's Bay, Labrador: $\delta^{34}S$, $\delta^{13}C$ and Se/S evidence. Econ. Geol. 97, 1307–1318.
Robinson, B.W., Kusakabe, M., 1975. Quantitative preparation of sulfur dioxide for $^{34}S/^{32}S$ analyses from sulfides by combustion with cuprous oxide. Anal. Chem. 47, 1179–1181.
Rooyen, V., 1954. Die geologie van.n gedeelte van gebied 7 (Potgietersrus). Geological Survey of South Africa, Pretoria (116 pp.).
Sharman, E.R., Penniston-Dorland, S.C., Kinnaird, J.A., Nex, P.A.M., Brown, M., Wing, B.A., 2013. Primary origin of marginal Ni–Cu–(PGE) mineralization in layered intrusions: Δ^{33} S evidence from the Platreef, Bushveld, South Africa. Econ. Geol. 108, 365–377.
Sharman-Harris, E., Kinnaird, J.A., Harris, C., Horstmann, U.E., Wing, B., 2005. A new look at sulfide mineralization of the northern limb, Bushveld Complex: a stable isotope study. Appl. Earth Sci. 114, B252–B263.
Smith, J.W., Holwell, D.A., McDonald, I., 2011. The mineralogy and petrology of platinum-group element-bearing sulfide mineralization within the grasvally norite–pyroxenite–anorthosite (GNPA) member, south of Mokopane, northern Bushveld Complex, South Africa. Appl. Earth Sci. 120, B158–B174.
Smith, J.W., Holwell, D.A., McDonald, I., 2014. Precious and base–metal geochemistry and mineralogy of the grasvally–norite–pyroxenite–anorthosite (GNPA) member, northern Bushveld Complex, South Africa: implications for a multistage emplacement. Mineral. Deposita 49, 667–692.
Thériault, R.M., Barnes, S.-J., 1998. Compositional variations in Cu–Ni–PGE sulfides of the Dunka Road deposit, Duluth Complex, Minnesota: the importance of combined assimilation and magmatic processes. Can. Mineral. 36, 869–886.
Truter, F.C., 1947. A Remarkable Transcurrent Fault near Potgietersrust. Geological Society of South Africa, Transvaal, pp. 501–515.
van der Merwe MJ (1978) The Geology of the Basic and Ultramafic Rocks of the Potgietersrus Limb of the Busveld Complex: Ph.D. Thesis (unpublished), South Africa, University of the Witwatersrand.
van der Merwe, M.J., 2008. The geology and structure of the Rustenburg layered suite in the Potgietersrus/Mokopane area of the Bushveld Complex. S. Afr. Mineral. Deposita 43, 405–419.
Villiers, D., 1967. The geology of the area south of Potgietersrus, with special reference to the chromite deposits Ph.D. thesis, University of the Witwatersrand (124 pp.).
Wagner, T., Boyce, A.J., Fallick, A.E., 2002. Laser combustion analysis of$\delta^{34}S$ of sulfosalt minerals: determination of the fractionation systematics and some crystal-chemical considerations. Geochim. Cosmochim. Acta 66, 2855–2863.
Westerlund, K.J., Gurney, J.J., Carlson, R.W., Shirey, S.B., Hauri, E.H., Richardson, S.H., 2004. A metasomatic origin for late Archean eclogitic diamonds: implications from internal morphology of diamonds and Re-Os and S isotope characteristics of their sulfide inclusions from the Late Jurassic Klipspringer kimberlites. S. Afr. J. Geol. 107, 119–130.
Yamamoto, M., 1976. Relationship between Se/S and sulfur isotope ratios of hydrothermal sulfide minerals. Mineral. Deposita 11, 197–209.